Astronomy & Astrophysics manuscript no. Mamonova_etal_revision2026b
May 11, 2026
©ESO 2026

arXiv:2604.20325v2 [astro-ph.EP] 8 May 2026

Stellar flare-driven evolution of primordial early exo-Earth atmospheres: Insights from a Young M Dwarf Flare model

E. Mamonova[1], K. Herbst[1], V. Kofman[1], O. Ozgurel[1], A. F. Kowalski[2,3,4], S. Wedemeyer[5,6], S. C. Werner[1]

[1] Centre for Planetary Habitability (PHAB), University of Oslo, 0315 Oslo, Norway
[2] National Solar Observatory, University of Colorado Boulder, 3665 Discovery Drive, Boulder, CO 80303, USA
[3] Department of Astrophysical and Planetary Sciences, University of Colorado, Boulder, 2000 Colorado Ave, CO 80305, USA
[4] Laboratory for Atmospheric and Space Physics, University of Colorado Boulder, 3665 Discovery Drive, Boulder, CO 80303, USA
[5] Rosseland Centre for Solar Physics, University of Oslo, 0315 Oslo, Norway
[6] Institute of Theoretical Astrophysics, University of Oslo, 0315 Oslo, Norway

Received 23 December 2025 / Accepted 15 April 2026

ABSTRACT

Context. M dwarfs are key targets for terrestrial exoplanet studies, with prospects for atmospheric spectroscopy. However, strong stellar magnetic activity and frequent flaring require modelling efforts to assess their impact on planetary atmospheres.
Aims. We aim to investigate one year of atmospheric chemical evolution of a young exo-Earth orbiting an active M dwarf by coupling our Young M Dwarfs Flare (YMDF) model of stellar activity with the VULCAN chemistry kinetic code.
Methods. The YMDF model provides time-resolved spectral energy distributions for high- and low-energy electron beam–driven flares, which are used as external radiative inputs to VULCAN to compute the time-dependent photochemistry and kinetics for different primordial atmospheric scenarios.
Results. We present the impact of stellar flares on atmospheres with varying water vapour content, ranging from a plausible primordial atmosphere with solar abundances, representative of a planet-forming region in a dissipating protoplanetary disk, to an extreme water-steam atmosphere with minimal other species. This was explored across several configurations: variable flux in the YMDF model, the previous model representing an active but older M dwarf with added 10K or 400K bottom boundary heat flux, and a constant stellar flux model.
Conclusions. Our study suggests that, compared to the previous model, the YMDF model produces synthetic flares that exert significantly greater stress on primordial atmospheres, regardless of the water-vapour content. Increased activity and prevalence of mid-size flares has the potential to induce permanent changes in atmospheric mixing ratios, especially in species with low abundances.

Key words. planets and satellites: atmospheres – stars: flare – stars: low-mass — methods: numerical

1. Introduction

M dwarfs are the most abundant stars in the solar neighbourhood and harbour the greatest number of exo-Earths within the liquid-water habitable zone (HZ, Owen 1980; Gaidos & Mann 2013; Dressing & Charbonneau 2015) compared to other stellar types. Therefore, they are prime targets in the search for terrestrial exoplanets. Their HZs lie at much smaller orbital separations than those around Sun-like stars, which enhances the geometric probability of detecting transits and increases the frequency of transit events. Crucially, these stars exhibit significantly higher magnetic activity levels, including frequent and energetic flares. During flare events, the M dwarf's luminosity in ultraviolet (UV), X-ray and extreme-UV (XUV) and visible wavelength ranges can increase by up to three orders of magnitude (Scalo et al. 2007). Our understanding of the activity of M stars has advanced considerably over the past two decades through high-precision, long-baseline photometric surveys such as Kepler (Borucki et al. 2010), K2 (Howell et al. 2014), and TESS (Ricker et al. 2015), which have provided an extensive statistical characterization of flare rates and properties across different stellar ages and types (Davenport et al. 2014; Davenport 2016; Hawley et al. 2014; Feinstein et al. 2024). Additionally, numerous UV and multi-wavelength studies using space-based observatories like the Hubble Space Telescope (HST) have complemented these surveys by capturing near-UV (NUV) and far-UV (FUV) flare emissions, revealing flare behaviour and energy distributions that are critical for assessing the impact of stellar activity on planetary atmospheres (Froning et al. 2019; Kowalski et al. 2019; Jackman et al. 2024; Paudel et al. 2024; Brasseur et al. 2023; Howard et al. 2019). These energetic stellar events primarily impact exoplanets orbiting M dwarfs, inducing significant photochemical alterations in their upper atmospheres (Segura et al. 2010; France et al. 2016; Tilley et al. 2019).

Studies of terrestrial planet atmospheres require a comprehensive understanding of their photochemistry. Unlike giant exoplanets, where composition is primarily perturbed by photolysis without surface emissions, terrestrial atmospheres arise from complex interplay among photolysis, reaction kinetics, vertical diffusion, escape, deposition, and condensation/sedimentation of condensible species, collectively controlling spectroscopically active trace gases whose lifetimes are governed by photochemical interactions (Hu et al. 2012). Whilst vertical diffusion, escape, and condensation also operate in gaseous planet atmospheres, the coupling of these processes with surface interactions and the absence of a deep thermal reservoir make terrestrial atmospheres particularly sensitive to their combined effects. After a protoplanetary disk dissipation, terrestrial planets may retain primary H_2-rich envelopes (Owen et al. 2020; Lis-

sauer et al. 2011), yielding atmospheres dominated by volatile hydrogen compounds or even water vapour (Miller-Ricci Kempton et al. 2012). The investigation of primordial atmospheres on terrestrial planets provides essential insights into the divergent evolutionary trajectories and habitability potential of rocky exoplanets.

In M dwarfs, stellar flares release energy in NUV and optical range (Paudel et al. 2024), and in the UV and extreme UV (EUV) wavelengths (France et al. 2016). Berger et al. (2024) found that the time-integrated energy ratio of FUV to NUV during flares is on average three times greater than what would be expected from a constant 9000 K blackbody spectrum. Due to the strong absorption of these high-energy photons, as planetary atmospheres tend to be optically thick in FUV and NUV, it results in significant energy deposition in the upper atmospheric layers, such as the thermosphere and exosphere (Kulikov et al. 2006; Segura et al. 2010). This absorption leads to heating at low pressures (high altitudes), while deeper layers receive minimal direct UV flux.

The NUV and FUV spectral regions are the primary drivers of photochemistry in planetary atmospheres, carrying sufficient photon energies to dissociate key molecules such as H_2O, CO_2, CH_4, and O_3. The exact role of NUV radiation in prebiotic chemistry on Earth remains uncertain (Ranjan et al. 2017), and M dwarfs may not emit sufficient quiescent NUV flux to drive such chemistry (Froning et al. 2019). However, their high flare frequencies deliver intense bursts across the FUV and NUV bands that could compensate for the low steady emission (Froning et al. 2019; Brown et al. 2023), making the time-averaged UV environment, particularly for young active stars such as AU Mic, a critical factor for both atmospheric photochemistry and the potential for prebiotic synthesis on orbiting planets.

Atmospheric escape from terrestrial planets orbiting active M dwarfs is driven by thermal processes, such as hydrodynamic outflows induced by XUV heating of the exosphere (Segura et al. 2010; Tilley et al. 2019; France et al. 2020; Modi et al. 2023; Luger & Barnes 2015), alongside non-thermal mechanisms including enhanced polar winds, ion pickup, and steady or transient stellar wind interactions (Ribas et al. 2016; Airapetian et al. 2017; Garraffo et al. 2017, 2022). In hydrogen-rich primordial atmospheres, the escape of light species such as molecular hydrogen may become diffusion-limited near the homopause, where upward fluxes are constrained by diffusion through heavier background gases under strong stellar irradiation (Kuramoto et al. 2013; Zahnle et al. 2020; Zahnle & Catling 2017; Katyal et al. 2020). Prior studies have quantified substantial losses, equivalent to several Earth oceans, for such atmospheres under young M dwarf irradiation, yet these calculations remain decoupled from the photochemical kinetics governing volatile replenishment and transformation (Yoshida et al. 2022; Luger & Barnes 2015). Coupled photochemical-kinetic simulations of primordial H-H_2O atmospheres, incorporating variable stellar fluxes, are thus required to interpret volatile retention and habitability potential.

Several studies have employed three-dimensional coupled chemistry-climate models to investigate the impact of stellar flares on rocky planet Earth-like atmospheres. Ridgway et al. (2023) coupled a general circulation model with photochemical kinetics to find that flares increase atmospheric ozone by a factor of 20. Chen et al. (2021) used observations to show that recurring flares drive atmospheres of K and M dwarf planets into chemical equilibria substantially deviating from their pre-flare states, with flare-driven transmission features of species such as NO_2, N_2O, and HNO_3 offering promise for future detection. Most recently, Chen et al. (2025) extended their framework to TRAPPIST-1 e, finding that flare frequency and spectral shape govern cumulative chemical changes, and O_3 variability strongly mediates atmospheric temperature responses. These 3D studies reveal important hemispheric and spatio-temporal variability of relatively quiescent or old M dwarf stars.

Complementary to these 3D studies, several authors have additionally investigated the photochemical response of hydrogen-dominated atmospheres to stellar flares using 1D and pseudo-2D models (Louca et al. 2023; Gibbs & Fitzgerald 2025; Konings et al. 2022; Nicholls et al. 2023). This difference in dimensionality is physically motivated: Earth-like atmospheres benefit from decades of observational constraints and well-validated 3D frameworks, whereas atmospheres of exotic compositions, with no direct Solar system analogue, remain far less observationally constrained, making a systematic 1D parameter survey a natural and necessary foundation for more complex future modelling. Such primordial H_2O-atmosphere simulations, achievable with a 1D photochemical-kinetic model assuming full stellar flux redistribution, could reveal the chemical processes controlling volatile retention and the habitability potential of young worlds orbiting M dwarfs.

A first step toward such studies is taken by investigating the chemical evolution of the water vapour primordial envelope of a 1 $M_\oplus$, 1 $R_\oplus$ rocky planet (hereafter referred to as early exo-Earth) orbiting a young, active early M dwarf such as AU Mic, at a separation allowing for an equilibrium temperature of ~500 K, representing an early, hot evolutionary stage rather than present-day surface habitability. While many earlier studies (see e.q. Segura et al. 2010; Tsai et al. 2023) have focused on short-term atmospheric responses or responses to individual flare events, and long-term simulations have to date addressed such compositions on tidally locked planets (see e.g. Chen et al. 2021), here we extend simulation timescales to capture the cumulative photochemical evolution of water-vapour-dominated atmospheres of terrestrial planets over approximately one year of repeated flare forcing. This duration balances the need to capture long-term chemical evolution with computational feasibility, allowing us to investigate both the direct effect and the long-term response of the atmosphere to the flares. We further evaluate how efficiently various species are transported to the upper layers of such primordial atmospheres by diffusion-limited escape. The manuscript is organized as follows: Section 2 describes the variable stellar flux model employed, the detailed parametrisation of the atmospheric grid and the chemical network of species along with vertical mixing parameters. In Section 3, we present a grid of atmospheric simulations evolved over approximately one year, comparing several configurations including constant quiescent flux. Section 4 places our findings in the broader context of planetary atmospheric evolution and habitability.

2. Methods

2.1. Simulations' setup

Our modelling focuses on the AU Mic system (Wittrock et al. 2023) with 0.5 $M_\odot$, 0.02±0.002 Gyr M dwarf, and its planet AU Mic d with a rotation period of 12.736±0.008 days. This planet is non-transiting and characterised by a known Earth-like mass determined by transit time variations (TTVs). AU Mic d orbits at a separation consistent with an equilibrium temperature of T_{eq} ~ 500 K under the current stellar luminosity, a value that will decrease as the star settles onto the main sequence and its bolometric output declines. The habitable zone around a typical

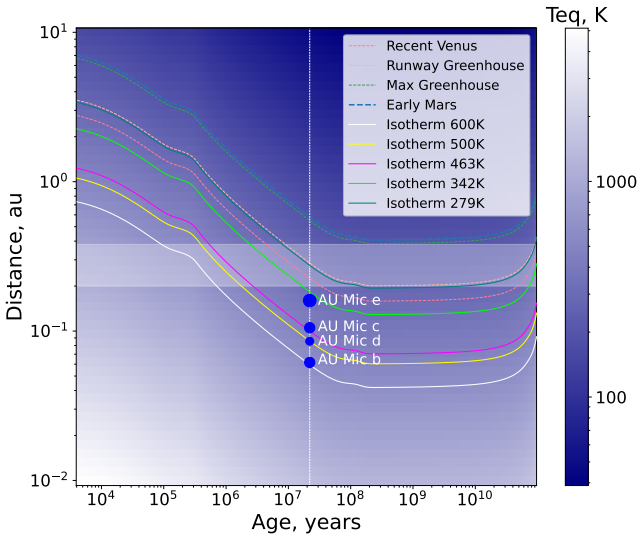

Fig. 1. Habitable zone evolution for M dwarfs with 0.5 $M_{\odot}$, showing planetary equilibrium temperature ($T_{\rm eq}$) and atmospheric condition shifts with stellar age. Calculated using MESA Isochrones and Stellar Tracks (MIST; Dotter 2016; Paxton et al. 2019). Dashed lines denote HZ boundaries (Recent Venus, Runaway Greenhouse, Maximum Greenhouse, Early Mars; Kopparapu et al. 2014); solid lines trace isotherms (600, 500, 460, 342, 279 K). Circles mark known exoplanets in the AU Mic system (22 Myr) across orbital separations.

M dwarf star evolves substantially during its pre-main-sequence contraction, shifting inward as the star cools and stabilises. Figure 1 illustrates this concept for the AU Mic system and HZ evolution around this 0.5 $M_{\odot}$ star, along with isotherms tracing changes in exoplanet equilibrium temperature. MIST isochrones (Dotter 2016) predict more temperate planetary conditions for d planet as its hosting M dwarf will enter the main sequence. Although the planet is non-transiting, this system is studied due to its well-characterised nature, serving as a template for other terrestrial planets orbiting M dwarfs; moreover, at a distance of 9.7 pc (Gaia Collaboration 2020), it ranks among the closer such systems and thus represents a promising target for future observations.

In a series of recent studies (Mamonova et al. 2025, hereafter Paper I, and Mamonova et al. 2026, hereafter Paper II), we introduced the Young M Dwarf Flare (YMDF) model, which characterises the spectral properties and temporal evolution of the flare activity in young M dwarfs. In this work, we use the synthetic spectra and temporal evolution data produced by the YMDF model as input to the atmospheric photochemistry. Considering the young age of the AU Mic system, we assume primordial atmospheres dominated by hydrogen with varying water vapour abundances.

To explore the influence of the atmospheric water content on flare-driven chemistry, we construct an atmospheric grid of 16 atmospheres spanning H_2O volume mixing ratios ranging from 0.1% to 100%, with the remaining composition scaled to solar elemental abundances, in two different regimes of internal heating: 10K and 400K. These two values of internal heating sample the edges of the physically plausible parameter space, from minimal interior heating to the hotter conditions theorised to allow ongoing silicate melting and magma ocean formation at the surface. Throughout this study, we compare the results of the chemical kinetic simulations within the grid of our atmospheres, that were subjected to variable stellar flux generated by our YMDF model, with those obtained using the framework described in Loyd et al. (2018), known as the 'fiducial flare' model (hereafter FF). Additionally, we perform simulations using a constant quiescent flux (CF) based on the AU Mic panchromatic flux. The simulations, incorporating interior heating of the atmosphere to 400 K at the lower boundary, are denoted as FF400K and YMDF400K, respectively. Different flare models enable a systematic assessment of varying UV fluxes on atmospheric composition and evolutionary trajectories, while probing the physically plausible parameter space extremes of interior heating.

2.2. Constructing the synthetic flare populations

We produced the population of flare events in form of an equivalent duration (ED, Gershberg 1972) distribution based on the broken power law relation with $\alpha_1 = 1.39$ and $\alpha_2 = 1.8$, found for AU Mic in Paper I. The broken power law function is mathematically expressed as:

$$f(x) = \begin{cases} A(x/x_{break})^{-\alpha_1+1} & : x < x_{break} \\ A(x/x_{break})^{-\alpha_2+1} & : x > x_{break}, \end{cases} \quad (1)$$

where A is amplitude, and x_{break} is the ED value at which the power law changes from coefficient α_1 to α_2.

Comparing to the observed flare frequency distribution (FFD), we added small flares to the population by choosing minimum ED smaller than observed and allow large flares by choosing maximum ED larger than observed. For producing a temporal evolution of stellar activity, we compare the obtained synthetic FFD to the observed AU Mic FFD (Paper I), and choose only populations passing a Kolmogorov–Smirnov (K–S) test, which assesses the null hypothesis that both samples are drawn from the same parent distribution. Using these conditions, we produced temporally resolved variable spectra in 36 chunks, each with a duration of 10 days, covering almost a year of stellar activity.

In Paper II, we simulated a synthetic spectrum of the stellar atmosphere during a flare event. This spectrum represents flaring on the entire projected surface area of the star. For each flare, the synthetic spectrum is scaled according to the flare's ED and represents the flux density at the peak of the flare. In physical terms, this corresponds to the flux emerging from the portion of the stellar surface that is actively flaring at the end of the impulsive phase. The temporal evolution of individual flares (i.e., spectra at timestamps before and after the peak) was then modelled using the flare time profile from Tovar Mendoza et al. (2022).

To put this work in context of the previous studies, we also produce stochastic flaring utilising the FF framework (Loyd et al. 2018; Loyd 2022) with the AU Mic's panchromatic spectrum (Feinstein et al. 2022) and its implementation of stellar activity. This enables us to evaluate the model-dependent effects of flaring on our atmospheric grid in the same timescale of 360 days. The FF framework enables the generation of light curves containing a sequence of flare events, where the frequency of flares is determined from the FFD, assumed to follow a single power-law:

$$f(>E) = \frac{\beta}{\alpha - 1} E^{-\alpha+1}. \quad (2)$$

Here we assume the power law coefficient α=1.8 and to be equal to the second coefficient α_2, calculated previously for AU Mic. This value of α is consistent with Loyd et al. (2018) results for active M dwarfs.

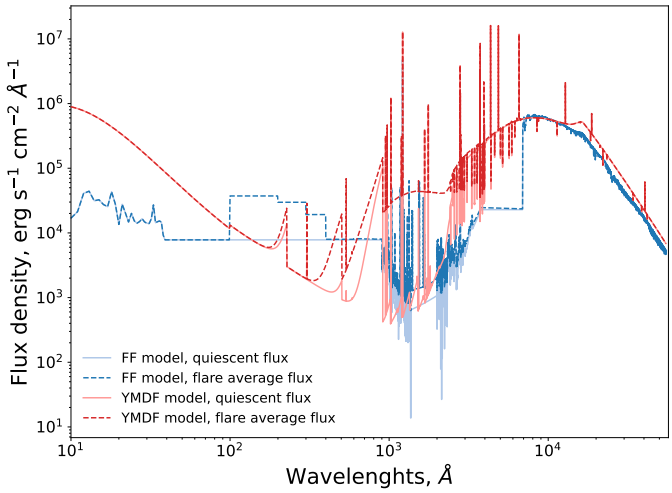

Fig. 2. Quiescent and averaged flux densities for the FF and YMDF models. Fluxes are shown for the quiescent state (solid lines) and simulation-averaged state (dashed lines), averaged over all flaring events contributions within 360 days for two flare activity models: YMDF model demonstrates a clear UV and NUV flux excess during flares compared to FF model, while longer wavelengths show good agreement across models and small excess in flux density comparing to the quiescent stellar radiation.

2.3. Synthetic flares

We produced the synthetic populations of stochastic flare events as described in Sect. 2.2, with the largest synthetic flare produced by the YMDF model possessing a bolometric energy of 6.575×10^{35} erg and a corresponding TESS band energy of 1.475×10^{35} erg. In contrast, the largest flare produced by the FF model yields bolometric and TESS energies of 1.061×10^{35} erg and 2.657×10^{34} erg, respectively. For the AU Mic star analysed in Paper I, we established flare occurrence rates above a cut-off energy of 10^{31} erg in the Kepler/TESS band, finding a daily rate of 14.3 flares at this threshold. Since more energetic flares follow the secondary power-law slope α_2 in the broken power-law distribution we found for this star ($\alpha_1 = 1.38$, $\alpha_2 = 1.8$, see Paper I for details), we recalculated the expected occurrence rates for flares at energies comparable to those of our model flares. Over the 360-day span of our simulation, the predicted cumulative rates for such energetic flares are 4.8 events in the FF model and 2.4 events in the YMDF model. These results imply that such flares are plausible within the modelled time frame and that our estimates may be on the conservative side. The flux density spectra of these flares produced YMDF and FF models are presented and discussed in Appendix A.2.

We computed the average flux densities over the 360-day period for two stellar flare activity models, FF and YMDF. In Fig. 2, we present the preflare (quiescent) flux alongside the average flux over this time span. Both models demonstrate enhanced emission in the UV and NUV regimes attributed to the flare events compared to quiescent flux, with the YMDF model producing a higher increase than the FF model. Deviations from the quiescent state are substantially reduced at longer wavelengths in both models. It is expected that M dwarfs flare activity predominantly increases energy input at the shortest wavelengths.

2.4. Temperature and pressure profiles

Following the modelling framework presented by Kempton et al. (2023), we adopt their approach to simulate hydrogen–helium–water atmospheres with variable water abundances. Specifically, we generate one-dimensional (1D) temperature-pressure (T-P) profiles in radiative-convective equilibrium using the open-source radiative-transfer code HELIOS[1] (Malik et al. 2017, 2019). Consistent with the aforementioned setup, we assume zero albedo and planet-wide heat redistribution, corresponding to a heat redistribution factor of 0.25 (heat is perfectly distributed over both hemispheres). In these calculation we used quiescent panchromatic flux of AU Mic (Feinstein et al. 2022) as before. We downloaded the opacity data used in this study from the Database for the Analysis of Complex Envelopes (DACE)[2]. Collision-induced absorption (CIA): H_2-H_2 and H_2-He pairs and Rayleigh scattering of H_2O, H_2, and He are included using established datasets and formulations (e.g., Borysow 2002; Richard et al. 2012; Crossfield & Kreidberg 2017; Sneep & Ubachs 2005). Including the scattering of water was done with consideration that the H_2O cross-section depends directly on the atmospheric abundance of water vapour.

The initial chemical compositions of the model atmospheres were computed under the assumption of thermochemical equilibrium using FastChem[3] (Stock et al. 2018), which efficiently determines equilibrium abundances for a wide variety of atomic and molecular species across relevant pressure and temperature ranges. In this work, we used FastChem to model 16 atmosphere abundances according to the adopted grid: we sample atmospheric compositions at 100, 60, 40, 25, 15, and 10% H_2O, repeating at one-tenth of these values successively down to 0.1% H_2O. The atomic abundances supplied to FastChem are scaled to reproduce each target H_2O mixing ratio by adjusting O/H accordingly, with C, N, and He depleted proportionally, anchored to solar values at 0.1% H_2O. These equilibrium abundances serve as the starting point for radiative-convective modelling with HELIOS.

The HELIOS code iteratively solves for 1D temperature-pressure profiles by balancing radiative transfer and convective adjustment, using a constant quiescent stellar flux. The code applies opacity data and allows for the self-consistent treatment of radiative-convective equilibrium (in this work, under cloud-free assumptions). The radiative transfer is implemented in a two-step process: first, the equilibrium T-P profile is determined using the k-distribution method with 20 Gaussian quadrature points in 384 wavelength bins spanning 0.244–500 μm, which ensures a sufficiently high resolution treatment of opacity. Then, the planetary emission spectrum is generated from the converged T-P profile using opacity sampling at spectral resolution $\lambda/\Delta\lambda$ =1000. For every atmospheric scenario, we employ "on-the-fly" opacity calculations weighted by the atmospheric abundances, calculated previously in FastChem.

Convection within the HELIOS framework is modelled using a convective adjustment scheme, which relies on the adiabatic coefficient governing the lapse rate in convective zones and the specific heat capacity. Therefore, we followed the approach by Malik et al. (2019), which utilizes ideal gas approximations.

In this study, we assume all temperature-pressure profiles are for cloud-free atmospheres. Given that water constitutes a significant fraction of these atmospheres, we verify the resulting profiles against the thermodynamic conditions for water condensa-

[1] https://github.com/exoclime/HELIOS
[2] https://dace.unige.ch/opacityDatabase/
[3] https://github.com/NewStrangeWorlds/FastChem

tion, either as liquid or solid. Throughout our model grids, all atmospheric conditions remain within the gaseous phase regime.

In Figure 3, we present T-P profiles computed with HELIOS for a hypothetical early exo-Earth planet orbiting our reference star AU Mic under quiescent stellar irradiation. Two interior heating scenarios are shown: low heating at 10 K (left panel) and high heating at 400 K (right panel). Convectively unstable layers are visually highlighted by the broader light grey shading, and indicate regions where the Schwarzschild criterion is violated; these layers are subject to convective adjustment within HELIOS calculations. Figure 4 illustrates the optical depth profiles on the wavelength-altitude diagram for two atmospheres, that represent the edges of our grid, 100% H_2O (left panel) and 0.1% H_2O (right panel). Key wavelength ranges accessible to current observatories are marked by the dashed vertical lines, including currently operating HST-COS in FUV and NUV (<3200 Å, Green et al. 2012), TESS[4] (6000–10500 Å, Ricker 2016), JWST instruments in near infra-red (NIR) and mid-IR (6000–288,000 Å, Kalirai 2018), decommissioned Kepler (4200–9000 Å, Borucki et al. 2010), and future ground-based ELT (3500–24500 Å, Padovani & Cirasuolo 2023) and space-based PLATO (4000-11000 Å, Rauer et al. 2025) facilities.

The flare energy release occurring at wavelengths shorter than 2464 Å is predominantly absorbed in the upper atmosphere at low pressures and high altitudes. Whether this partial UV deposition has a measurable effect on the temperature-pressure profile is examined below, in Sect. 3.3.

2.5. Averaged flare flux

In order to determine whether the addition heating of the upper atmosphere layers is present, we further analysed the impact of the flux of flaring star averaged over the total simulation time compared to the quiescent flux in the solar abundance atmosphere containing 0.1% H_2O. The T-P profile were computed using the k-distribution method as before, calculating over 9,213 wavelength bins spanning 0.02–200 μm, and we refer to it as the UV setup hereafter. The planetary emission spectrum was generated from the converged T-P profile using opacity sampling at the same spectral resolution, $\lambda/\Delta\lambda = 1000$. This approach allowed us to focus on a treatment of UV opacities while enabling to omit collision-induced absorption, which primarily occurs at greater atmospheric depths where pressures are sufficiently high. Our goal is to assess whether the additional heating will be present in the upper atmospheric layers, that could accelerate atmospheric escape processes and influence mixing dynamics. For opacities calculations in HELIOS, we used the averaged flux densities computed in the YMDF model. The choice was motivated by the fact that the YMDF model yielded an average integrated flux over the 360-day period of $\sim 1.0 \times 10^{10}$ erg s^{-1} cm^{-2} Å^{-1}, which exceeds the corresponding value of $\sim 0.7 \times 10^{10}$ erg s^{-1} cm^{-2} Å^{-1} for the FF model. As our goal was to investigate whether the temperature-pressure profile changes significantly under an increased flux, we thereby selected the model with the higher energy input.

The left panel of Fig. 5 illustrates the optical depth profile (in the UV setup) of the 0.1% H_2O atmosphere irradiated by the flare-average flux from AU Mic, our reference for a flaring young M dwarf. The right panel compares several T-P profiles: the 0.1% H_2O atmosphere under quiescent and flare-averaged fluxes in the UV setup; the wavelength grid T-P profile used throughout this study; a profile for the same atmosphere with an additional 400 K interior heating; and a mini-Neptune profile with a similar surface gravity to Earth ($\log g = 3.0$) and the equilibrium temperature of 500K from Kempton et al. (2023), consistent with the parameters adopted in our study. The T-P profiles computed in the UV setup do not significantly deviate from the T-P profile adopted in this study, particularly in the upper atmospheric layers where photochemical processes predominantly occur. This confirms that the flare energy deposited at wavelengths shorter than 2464 Å affects predominantly the upper atmosphere at low pressures and high altitudes, leaving the deeper atmospheric layers largely unaffected. The discrepancies observed in the lower layers can be attributed to our exclusion of CIA effects from H_2-H_2 and H_2-He pairs, as these processes are not influenced by UV radiation. This simplification reduces computations and allows the layers to converge within the adequate simulation runtime.

2.6. Chemistry kinetic code setup

The atmospheric chemical kinetics are modelled using the VULCAN[5] code (Tsai et al. 2017, 2021), a 1D thermochemical solver that tracks atmospheric species evolution across diverse temperature and pressure conditions. VULCAN solves the coupled continuity equations for a network of chemical reactions, incorporating photochemistry, thermochemistry, vertical mixing, and molecular diffusion, thereby capturing the interplay between stellar irradiation and atmospheric composition.

We adjust the VULCAN code to work with variable stellar flux[6]. Triggered by the flare event, the atmosphere is being rebuilt with the changing flare flux at every time step. At the start of the flare event, the integration time step is minimized to enable the atmospheric chemistry to respond rapidly to changes. The time step sizes are controlled adaptively based on an estimate of the truncation error, which typically decreases over time, allowing for progressively larger steps as the system evolves toward numerical steady state as defined in Tsai et al. (2017). To ensure that no flare spectra are missed during the integration, the maximum permissible time step is limited to the interval between the current simulation time and the onset of the next flare event.

In this study, we utilised the N-C-H-O full photochemical kinetics network, which includes nitrogen-, carbon-, and oxygen-bearing species for computing chemical reaction rates. The atomic abundances supplied to FastChem follow the atomic abundance scaling described in Sect. 2.4, where O/H is adjusted to reproduce each target H_2O mixing ratio and the remaining species are depleted accordingly. The initial mixing ratios for selected atmospheric setups are presented in Fig. B.1 in Appendix B.3. Photochemical reaction rates are determined based on the local flux density at each layer, incorporating species-specific cross sections. Thermal reaction rates are computed simultaneously, reflecting the local temperature-dependent kinetics. Both types of reactions are evaluated continuously for every layer given stellar flux variability as we described above.

2.7. Vertical mixing

Determining an accurate diffusion coefficient presents a significant challenge in modelling atmospheric mixing. In the adopted framework, atmospheric mixing in the vertical direction is represented by both eddy and molecular diffusion. Eddy dif-

[4] http://www.nasa.gov/tess-transiting-exoplanet-survey-satellite

[5] https://github.com/exoclime/VULCAN

[6] https://github.com/cepylka/vulcan-flares

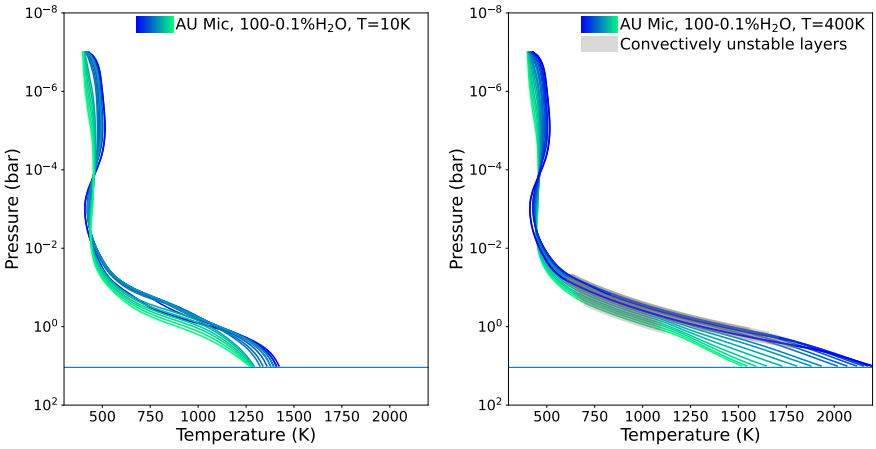

Fig. 3. Temperature and pressure profiles (x- and y-axis, respectively) for two interior heating scenarios: 10 K (left panel) and 400 K (right panel), computed for quiescent AU Mic irradiation. The profiles represent a hypothetical early exo-Earth with 1 $M_\oplus$, 1 $R_\oplus$ located at an orbital distance producing an equilibrium temperature of 500 K. The atmospheric grid spans primordial compositions with water vapour abundances ranging from 100% down to 0.1%, with the remaining fraction composed primarily of hydrogen and helium at solar abundances. Convective zones are displayed as broader light grey shadowed lines. All atmospheric structures were self-consistently calculated using the HELIOS code from equilibrium state reached in Fastchem.

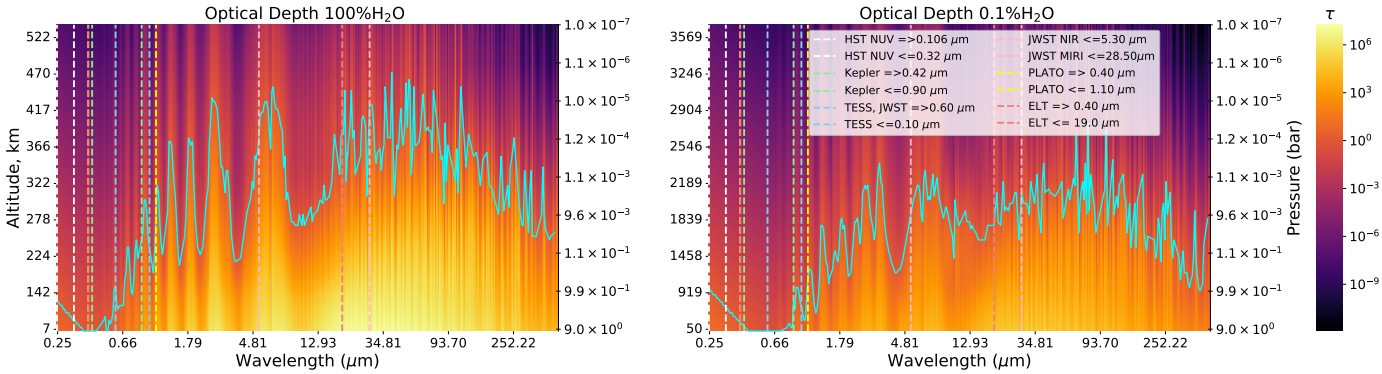

Fig. 4. Optical depth profiles for the atmospheres with H_2O concentrations of 100% and 0.1%, calculated using HELIOS (left and right panels, respectively). Light blue lines represent the optical depths $\tau \sim 1$, while the colour map shows varying τ values across the atmospheres. The x-axis shows wavelength and the y-axis indicates altitude (left) and pressure (right). Dashed vertical lines mark the observational ranges accessible by instruments onboard the HST (COS, <0.32 μm), Kepler (0.42–0.90 μm), TESS (0.60–1.05 μm), JWST [NIRCam (NIR): 0.60–5.00 μm, MIRI (MIR): 5.00–28.8 μm]. Future telescope ranges are stated for ELT (0.35–2.45 μm) and PLATO (0.40–1.10 μm).

fusion generally dominates in the lower and intermediate atmospheric layers, where species are relatively well mixed.

In a typical 1D model, the eddy diffusion coefficient, K_{zz} is often estimated using a mixing-length theory (MLT) approach, given by $K_{zz} = Clw_t$, where C is a constant, l is the mixing length, and w_t is the turbulent velocity, under the assumption of free convection. For H_2-dominated atmospheres, a range of models Parmentier et al. (2013); Moses et al. (2013); Miguel et al. (2015) utilize Kzz values between 10^8 and 10^{12} cm^2 s^{-1}. In this study, the K_{zz} from Moses et al. (2022) and Louca et al. (2023) is adopted:

$$K_{zz} = 5 \times 10^8 \left(\frac{P}{1\ \mathrm{bar}}\right)^{0.5} \left(\frac{H_{1\ \mathrm{mbar}}}{620\ \mathrm{km}}\right)\left(\frac{T_{\mathrm{eff}}}{1450\ \mathrm{K}}\right)^4 \quad (3)$$

where P is the atmospheric pressure in bars, $H_{1\ \mathrm{mbar}}$ is the scale height at 1 mbar, and T_{eff} is the effective temperature. For more detail, see Appendix A.5.

In the uppermost atmospheric regions, mixing is primarily due to molecular diffusion. Layer-related vertical molecular diffusion coefficients D_{zz} are adopted from Moses et al. (2000), and selected based on the dominant species. Water vapour is considered dominant in atmospheres with 40–100% H_2O, while for the rest of the grid, H_2 is the main constituent.

Boundary conditions are specified as follows: the lower boundary is closed (no net flux), while the upper boundary allows for diffusion-limited escape of particles into the exosphere. The surface is treated as a solid boundary, and thermal coupling with the interior is included through the lower boundary temperature. A diffusion-limited flux defines the maximum rate at which particles escape, governed by their rate of diffusion upward into the exosphere, thereby providing an upper bound on potential atmospheric escape rather than a self-consistent escape rate. Further discussion of boundary effects and escape mechanisms appears in Sect. 3.3.

3. Results

3.1. Cumulative changes in water vapour atmospheres of early exo-Earths

The flare activity response was studied across our grid of water vapour atmospheres. By analysing these relatively long-term changes in comparison to the typical timescales of atmospheric processes, we characterise how sustained flare forcing reshapes their chemical composition and vertical structure. We first describe the end-state atmospheric compositions across the water vapour grid, and then examine the time-dependent behaviour of key species in the upper atmosphere.

In Figure 6, we present the chemical compositions of four atmospheres of different in water fractions in columns, while the stellar activity regimes are arranged by rows: the YMDF, FF, FF400K models, and the CF model characterised by a constant stellar flux. Each panel depicts the mixing ratios of key species after 360 days of chemical kinetic integration or upon reaching the numerical steady state, whichever occurs first. Notably, the

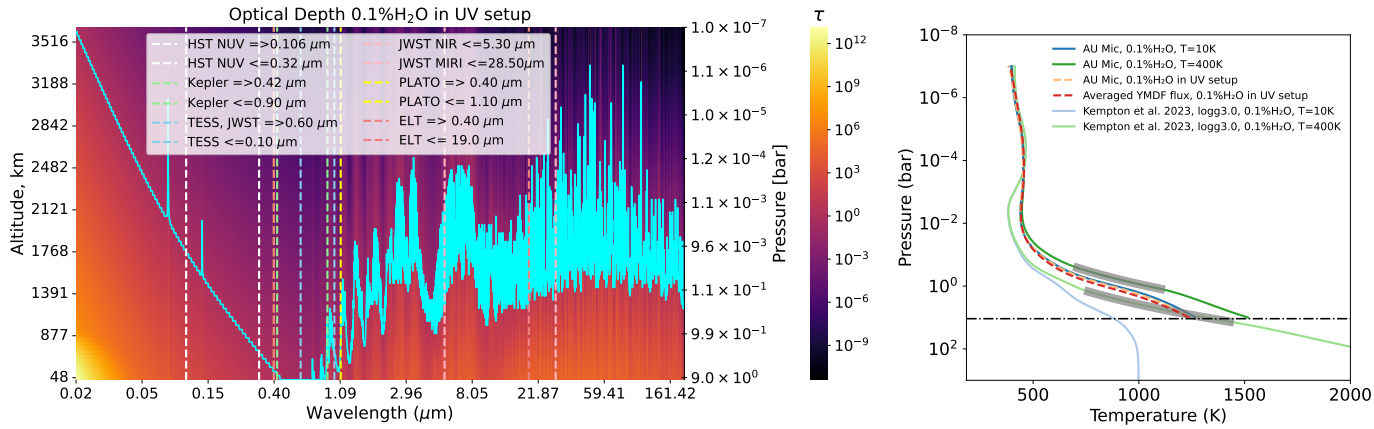

Fig. 5. UV setup implementation for optical depth and TP profile calculations. Left panel: optical depth profile for a 0.1% H_2O atmosphere irradiated by the average flux from AU Mic, representing a flaring young M dwarf reference. As before, the colour map shows varying τ values across the atmospheres with light blue line as $\tau \sim 1$. Right panel: comparison of T-P profiles, including: the UV setup profiles for the 0.1% H_2O atmosphere under quiescent and flare-averaged fluxes (dashed orange and red lines, respectively); the T-P profile based on a wavelength grid used throughout this study (solid blue line); the same atmosphere heated by an additional 400 K from the interior (solid green line, the light-green shadowed area denotes convectively unstable layers); and a mini-Neptune T-P profile with surface gravity comparable to Earth from Kempton et al. 2023 (solid light-blue line).

steady state solution was achieved only for H_2-dominated atmospheres under the constant flux regime, requiring between 100 and 222 days (the shortest time observed for simulations with 10% H_2O and the longest for those with 0.25% H_2O).

At the high H_2O content, in the YMDF and CF models, photodissociation of water by intense radiation continuously produces H and O, with molecular and atomic oxygen accumulating in the upper atmosphere. In contrast, the FF model with frequent, low-energy flares maintain persistently perturbed upper layers of the atmosphere, dominated by hydrogen species. The continuous small flares prevents the atmosphere from recovering between events, suppressing the build-up of oxygen species. At lower H_2O content, all models exhibit high mixing ratios of hydrogen species throughout the atmosphere at all altitudes. In these atmospheres, the profiles of pressure and mixing ratios for species such as CO_2, and CH_4 appear similar across models, with the exception of the YMDF model, which predicts slightly higher concentrations of CO_2, and lower levels of methane in the upper atmosphere. CO number densities are generally slightly elevated in hydrogen-dominated atmospheric compositions under the YMDF model, whereas in the 100% H_2O atmosphere the YMDF and CF model yield noticeably lower CO abundances compared to the FF models. The YMDF and CF models allow oxygen species to persist in the upper atmospheric layers, reflecting differences in the time-resolved flare forcing on the atmosphere. These results demonstrate that the FFDs of stellar flares play a critical role in governing the long-term redox balance of primordial atmospheres under sustained stellar irradiation, and underscore the necessity of incorporating stellar flare statistics into the interpretation of exoplanetary spectra.

The lower layers of the atmosphere influenced by the interior heating in the FF400K model show that species such as H, H_2, H_2O, and He remain largely unaffected, whereas atomic oxygen and O_2 are present in increased abundances, and methane is depleted at this depths throughout the grid of the water vapour concentrations, if compared to simulations without internal heating in the FF and CF models. It highlights that the heating conditions at the lower boundary primarily affect the deeper parts of the atmosphere, altering the abundances there. Nonetheless, in the investigated grid of atmospheres, the mixing ratios in the upper atmosphere remain largely unaffected by the interior heating, indicating limited coupling between temperature-dependent kinetics in the lower atmosphere and photolysis-driven chemistry in the upper atmosphere. We additionally examined the absolute number density profiles across all models and for two extreme compositions (100% and 0.1% of water content), finding agreement with the mixing ratio analysis presented above. The number density profiles, together with further discussion, are provided in Appendix B.2 and Fig. B.2.

The temporal evolution of the mixing ratios of photodissociation-driven species in the uppermost atmospheric layer are presented in Fig. 7 at the upper (100%) and lower (0.1%) extremes of water content, arranged by columns, while the rows correspond to the models. All models with variable stellar flux input exhibit rapid changes in species mixing ratios associated with flares, while the CF model, after some initial variation, stabilises to constant mixing ratios as expected. The YMDF and FF models effectively produce and transport H to the uppermost atmospheric layers, where it becomes available for diffusion-limited escape. The FF and FF400K models produce very similar results regardless of water content, suggesting that the photochemical composition of the upper atmosphere is not significantly influenced by interior heating.

In the uppermost layer of the 100% H_2O atmosphere, H_2 reaches mixing ratios of 0.01–0.20 in the FF and FF400K models, whereas it remains at trace levels in the YMDF and CF models. The CF model sustains high O_2 with some atomic O, minimal H_2, and ~20% atomic H over one year, while the FF is dominated by H (~70%) and H_2 (~30%). The YMDF shows interchangeable O and O_2 abundances (20–60%), reflecting dynamically stressed conditions from mid-sized flares. In the 0.1% H_2O case, water mixing ratios hover around 10^{-5} across variable flux models (slightly higher, $> 10^{-4}$, in CF), with H and H_2 dominant; the YMDF uniquely exhibits sporadic atomic O ($\sim 10^{-4}$) from flares, and H_2 lower than others. Across the grid, water vapour is efficiently reduced to ~1% of initial values there, driven by both flare activity in all variable flux models, and, to a somewhat lesser extent, under constant stellar flux.

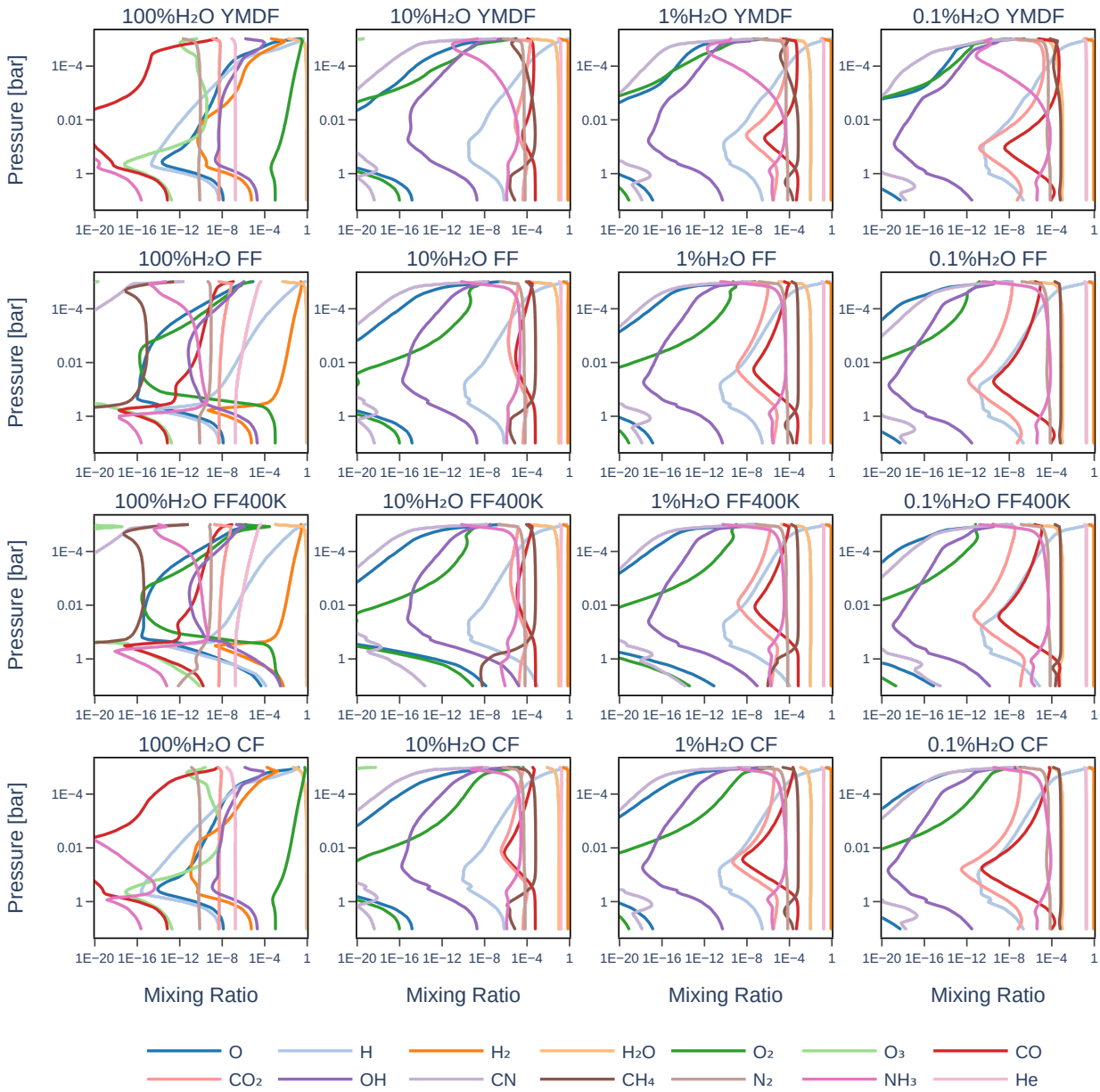

Fig. 6. Atmospheric chemical compositions after one year of simulation time for four atmospheres with water fractions of 100%, 10%, 1%, and 0.1% arranged by columns, and four stellar forcing regimes arranged by rows: the YMDF, FF, FF400K, and the CF models. Each panel shows the mixing ratios of key species after one year of chemical kinetic integration. In the constant flux regime it was allowed to the system to achieve a numerical steady state, if occurs before one year period. See supplementary animation (DOI:10.5281/zenodo.18029710, in prep.) for 16 atmospheres under the YMDF model flaring.

Our simulations reveal that atmospheres comprised almost entirely of water vapour (we denoted it as 100%H_2O) under the YMDF and CF models exhibit significant amount of molecular and atomic oxygen in the uppermost layer. Interestingly, the FF and FF400K models results indicate a markedly different atmospheric composition at higher altitudes. Here, atomic and molecular hydrogen rapidly dominate the upper layers of the atmosphere, along with a dramatic depletion of oxygen species to parts-per-billion (ppb) levels, leaving permille concentrations only in the lower part of the atmosphere. The atmospheres affected by the YMDF model output exhibit the presence of atomic O up to 10^{-4} concentrations even in solar abundances atmosphere (0.1%H_2O). This stark divergence suggests that the increased production of low-energy flares profoundly alters the upper atmospheric chemistry, which can be understood in terms of the balance between radical species production and recycling. Photodissociation of water ($H_2O + h\nu \rightarrow H + OH$) provides the primary source of hydrogen radicals, which rapidly recycle hy-

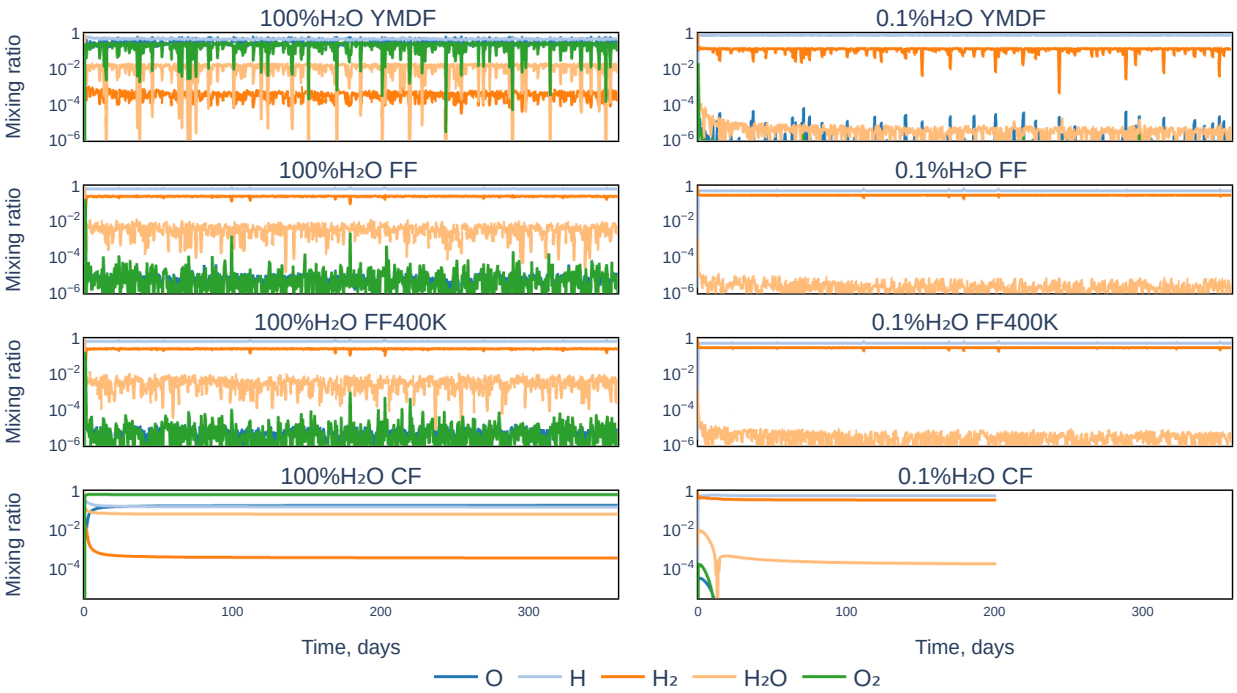

Fig. 7. 360-days evolution of the mixing ratios of photodissociation-driven species with concentrations above 10^{-4} in the uppermost atmospheric layer are shown for four atmospheres with water fractions arranged by rows: 100%, 10%, 1%, and 0.1%. The left and right columns correspond to the YMDF and FF models, respectively. Each panel presents the temporal evolution of species mixing ratios over the span of one year, with the y-axis showing mixing ratio and the x-axis representing time. The CF model at 0.1%H_2O shows the temporal evolution until the model reaches a steady state at day 201 of the simulation.

drogen through reactions forming H_2 and other reduced species. In the YMDF scenario, episodic high-energy flare events enhance photolysis rates and increase the production of atomic oxygen, facilitating the build-up of O and O_2 in the upper atmosphere. In contrast, the frequent but lower-energy events in the FF scenario maintain a more hydrogen-dominated radical environment, where oxygen radicals are more efficiently recycled back into water or other reduced species, limiting the accumulation of oxidised products. Therefore, the frequency and distribution of stellar flares can be crucial factors influencing the production or inhibition of oxygen species in primordial atmospheres.

To further explore the effect of additional interior heating on the atmospheres, we simulated 100% and 0.1% H_2O atmosphere scenarios with an interior heating of 400K in the YMDF model, shown in Fig. B.8 in Appendix B.4. The additional heating accelerates reaction kinetics in the lower atmosphere, with most changes compared to the model without interior heating occurring there. Hydrogen and oxygen species have slightly elevated mixing ratios there. In the upper layers, changes are negligible with the exception of the uppermost layers, where the lower right panel of the figure reveals a sporadic presence of both O and O_2 at mixing ratios around $\sim 10^{-4}$, analogous to atmospheres without additional interior heating. For further discussion and additional analyses, see Appendix B.4.

3.2. Spontaneous flare-induced changes in water vapour atmospheres of early exo-Earths

In water-rich compositions, H_2O itself contributes significant opacity in the ultraviolet, acting as a self-shielding species that buffers photolysis rates at higher pressures even when the incident NUV/FUV flux varies appreciably. Additional absorbers, such as CO_2 or hydrocarbons, may further modulate the penetration of short-wavelength radiation into deeper atmospheric layers. In the 100% H_2O atmospheres, water shows effectively no changes in the mixing ratios except for uppermost layers due to shielding; however, the initially low H_2 concentrations react remarkable different in this regime under the YMDF and FF activity models. In the former H_2 concentrations are visibly disturbed by flare activity, and in the latter, it slowly accumulates in the upper and middle atmosphere, as shown in Fig. 8. This behaviour can be understood as follows: species with low mixing ratios are particularly susceptible to flare-driven perturbations, an effect most pronounced under the YMDF model where mid-sized, energetic flares perturb trace species across a broad altitude range. Conversely, species gained higher mixing ratios by efficient background production show little or no detectable response under the FF model, where predominantly low-energy flares are insufficient to overcome background production rates.

The magnitude and vertical distribution of photolysis rates are governed by the wavelength-dependent actinic flux that directly reflect changes in the stellar flux due to flare activity, and the absorption cross-sections of the dominant atmospheric species (see Appendix A.3 for details). In the upper atmosphere,

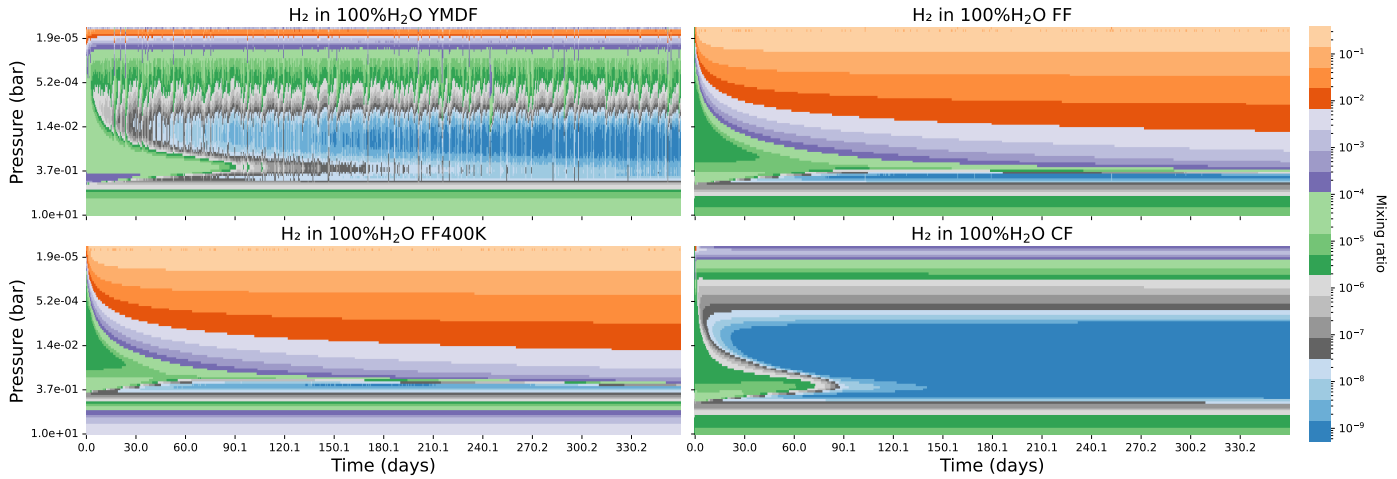

Fig. 8. Time evolution of H_2 mixing ratio for an atmosphere with 100% H_2O. The heatmaps display vertical profiles over the 360-day simulation duration, with pressure (in bars) on the y-axis and time (in days) on the x-axis. The upper row shows results from the YMDF and FF models, while the bottom row corresponds to the FF 400 K and the CF model, as indicated on the panels.

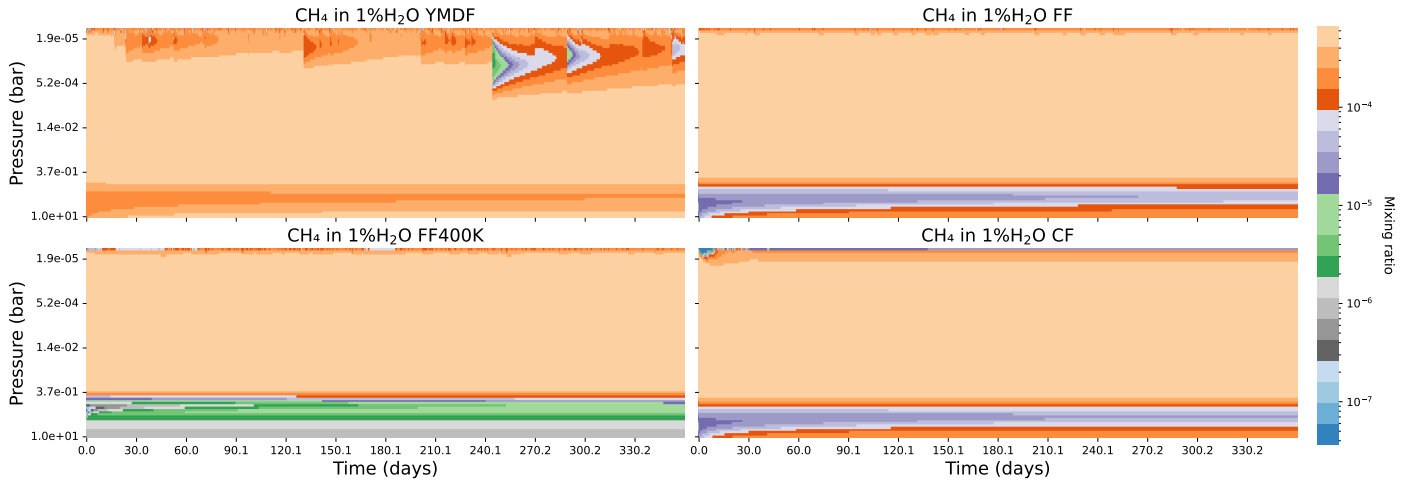

Fig. 9. Heatmaps of CH_4 mixing ratio in the atmosphere with 1% H_2O over the 360-day simulation period for an atmosphere containing 100% water vapour analogous to the previous Fig. 8

variations in the stellar UV flux during flare events produce noticeable changes in photolysis rates for several species (see Fig. A.2); however, deeper in the atmospheric column, strong UV shielding substantially suppresses any further enhancement of photolysis rates. The enhanced CH_4 abundances in the lower atmosphere under the YMDF model are consistent with flare-driven vertical redistribution from upper to lower layers, whereas in the FF model, persistent but shallow radical production depletes upper atmospheric CH_4 without significantly perturbing the deeper layers beyond the state established by the quiescent flux. The FF400K case shows even stronger CH_4 depletion at depth, which hints on thermal nature of this effect.

The four panels in Fig. 9 represent heatmaps of the methane evolution in 1% H_2O vapour atmospheres. The results reveal a pronounced response of the CH_4 mixing ratio to the flare input of the YMDF model corresponding to the most energetic flare event (at 243.671 day of the simulation), characterised by sharp temporal variations. Although a full return to preflare conditions is not observed within that the simulation timespan, it is inferred that the atmosphere would eventually re-equilibrate given the clear trend in the mixing ratio, if we assume the absence of subsequent large flares. However, this recovery is likely to be interrupted by the first successive very energetic flare. Longer simulation durations would be required to confirm this behaviour conclusively.

In contrast, the atmospheric response to the FF model stellar flaring, shows limited response to the most energetic flare in the model (at the 136.069 days of the simulation) under these conditions. However, as demonstrated in Fig. B.3, the temporal evolution of O_2 in the 10% H_2O atmosphere reveals that the response to flare activity remains pronounced in the FF model as well. When we consider the FF400K model, the atmospheric response to flares becomes more pronounced, suggesting that increased thermal conditions at the bottom of the atmosphere amplify the chemical perturbations induced by stellar activity by increasing reaction rates and vertical mixing. Both panels for the response on the FF and FF400K models show that slightly less methane accumulate in the lower atmosphere, and with introduced interior heating the effect is more pronounced. The response to the CF model displays the evolution of CH_4 with reaching a steady solution at ~209 day under stable stellar forcing conditions. An analogous atmosphere response was observed in the temporal evolution of ammonia (NH_3) mixing ratios (see Fig. B.4 in Appendix B). For these two species, the long-term response to the largest flares in the corresponding simulations is pronounced throughout our atmospheric grid, with the excep-

tion of the 100% H_2O atmosphere, where the high abundance of water vapour suppresses the other species to minimal concentrations, preventing their accumulation over the duration of the simulation. This behaviour emerges as larger portions of the atmosphere approaching solar abundances due to decreasing water content. The effect similar to the persistent changes in CH_4 and NH_3 across all water concentrations in hydrogen-dominated atmospheres (H_2O < 40%), is also observed at somewhat lesser extent in other species including CO, CO_2, H, and OH under stellar forcing of the YMDF model (see Fig. B.5 in Appendix B). Reduced species such as CH_4 and NH_3 are particularly sensitive to flare-driven photochemistry, as they are efficiently destroyed through reactions with radical species produced during water photolysis, leading to their rapid conversion into the reactive intermediates CH_3 and NH_2.

Water abundance is exceptionally uniform throughout the atmospheric grid and models, showing a comparable decrease in mixing ratio at higher altitudes, with the sole exception of the 0.1% H_2O atmosphere under the YMDF model, where self-shielding likely becomes ineffective under sufficient stellar flaring (see Fig. B.6 in Appendix B). Here, the strongest flare in the simulation induces atmospheric reactions observable possibly attributable to the minimal water content in this atmosphere. Consequently, across the grid, water vapour acts as the stable and primary source of opacity in the relevant atmospheric layers, emphasising its dominant role in controlling radiative transfer processes within these environments, while H_2 contributes through CIA, and He contributes through Rayleigh scattering and CIA in combination with H_2. We additionally find that the mixing ratio of H_2 remains largely stable from atmospheres with 60% H_2O down to 0.1% H_2O, except in the uppermost layers where dynamics are observed, even in the CF model.

3.3. Diffusion limited escape

The upper layers of the atmosphere are available for particle escape driven by both thermal and non-thermal mechanisms, including hydrodynamic outflow caused by X-UV and EUV heating, as well as non-thermal escape such as sputtering, charge exchange from stellar winds, and photochemical losses. In our modelling framework, the atmosphere is simulated in the pressure regime from bottom 10 bar to top 10^{-5}. This upper boundary lies near the exobase, the altitude where the atmosphere transitions from collisional to collisionless flow and where escape mechanisms become dominant. We, therefore, focus on the diffusion-limited escape regime where molecular and eddy diffusion control species transport. The escape of light species (e.g., H, H_2, He) can be limited by their availability at the top of the atmosphere; this supply is modulated by vertical diffusion from the homopause (Tsai et al. 2021), leading to a diffusion-limited escape with the flux:

$$\Phi_{\rm DL} = D_t n_i \left(\frac{1}{H_t} - \frac{m_i g}{N_{\rm Avo} k_B T} \right) \tag{4}$$

where $\Phi_{\rm DL}$ denotes the diffusion-limited flux, D_t is vertical molecular diffusion coefficient D_{zz} calculated for the uppermost layer, n_i is the number density of species i there, H_t is the scale height and T is the temperature, all evaluated at the top of the atmosphere, m_i is molecular mass of species i, and the constants $N_{\rm Avo}$, and k_B represent the Avogadro's constant and Boltzmann's constant, respectively. We note that the direct proportional relationship between diffusion-limited flux and number density should be noted. Additional information is presented in Appendix A.6 for completeness.

Figure 10 shows the diffusion-limited escape rates averaged over the 360-day period for key atmospheric species across a broad spectrum of atmospheres characterised by water vapour concentrations from 100% down to 0.1%, for the YMDF, FF (left and centre panel, respectively) along with the CF model (right panel). This figure reflects the upward flux at the uppermost atmospheric layer, weighted by the species-specific thermal diffusion factor α (see Appendix A.6) and the local number density, and is intended to inform expectations for layers closer to the exobase rather than to quantify escape rates directly. Therefore, it characterises the reservoir of atmospheric species available for loss below the exobase.

Wider envelopes, representing the a standard deviation from the mean values, indicate enhanced variability resulting from species intermittently moving into and out of the upper layer. When species momentarily leave, the mixing ratio can approach zero, causing fluctuations. Conversely, narrow envelopes signify a stable, continuous presence of species, indicating uninterrupted availability for diffusion-limited escape.

The variability with H_2O content in all models arises from the ability of even the quiescent AU Mic flux (CF model) to photodissociate water, driving an intermittent production of O, O_2, and OH in the upper layers; atomic C is also marginally affected but remains at low number densities due to rapid conversion into more complex carbon-bearing species. The stark transition between the 100% and 60% H_2O regimes reflects the shift from a water-dominated atmosphere, where all other species exist only at trace abundances, to a compositionally richer regime where H, He, C, N, and O are more substantially represented, though still following solar ratios within the non-water fraction. Under the YMDF model, energetic flares drive enhanced photodissociation of H_2O, producing greater variability in oxygen-bearing species, whilst H_2 shows the largest variability, reflecting the stronger overall atmospheric stress. The FF model, by contrast, shows greater relative variability in O and O_2, as its predominantly low-energy flares incrementally perturb oxygen radical abundances without imposing comparable stress on H_2. Towards the 0.1% H_2O end of the grid, hydrogen-bearing species converge across models, however, in the CF model H_2 replaces atomic H as the dominant escaping species, whilst flaring models continue to dissociate H_2 and transport atomic H upward. The systematically lower upward flux of oxygen-bearing species in FF relative to YMDF reflects the less effective production of O, O_2, and OH under low-energy flaring.

4. Discussion

4.1. Primordial atmosphere of an early exo-Earth

The population of known terrestrial exoplanets orbiting very young M dwarfs at ages of 5-10 Myr remains sparse, primarily due to the observational challenges posed by these super-young and highly active systems (Newton et al. 2016; Andersen & Korhonen 2015). Such stars are often embedded in dusty environments and exhibit intense magnetic activity, which complicates detection and characterization efforts. Consequently, empirical constraints on the atmospheric compositions and evolutionary pathways of terrestrial planets in these nascent systems are limited.

The most important constituent in the explored grid of atmospheres is water, owing to its pivotal influence on habitability as well as atmospheric radiative properties and photo-

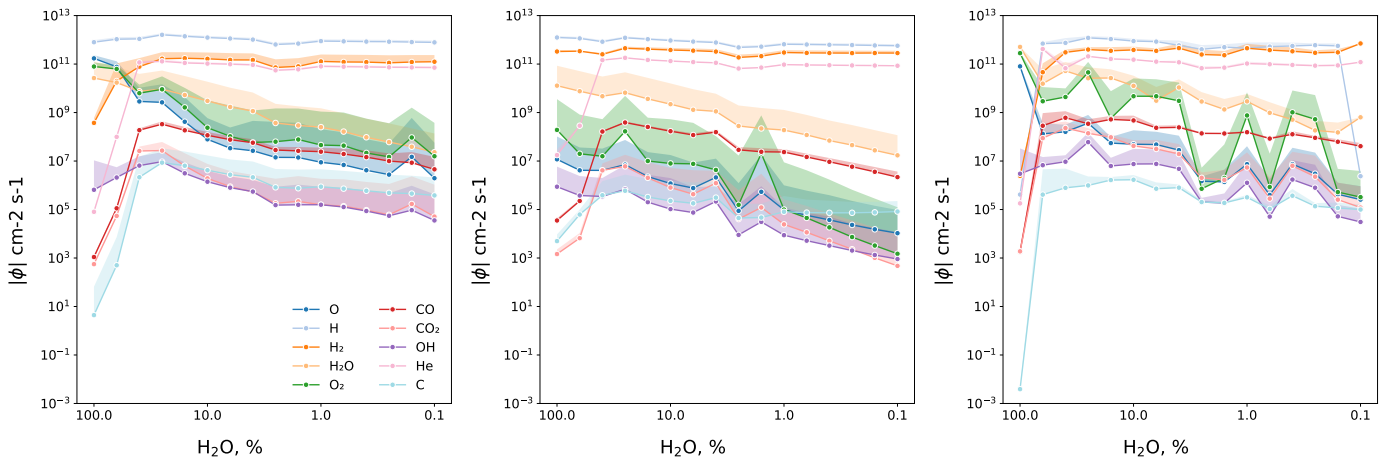

Fig. 10. Diffusion-limited escape averaged over one year for the principal atmospheric species across a range of atmospheres with water vapour concentrations varying from 100%-0.1%. The left panel shows results of the calculations using the YMDF variable flux, the centre panel presents the FF model application, and the right panel shows averaged rates for the simulation with the constant stellar flux. The coloured envelopes show the standard deviation of the upper bounds only; the lower bounds are omitted for clarity as they are symmetric.

chemical pathways. Our results therefore characterize the atmospheric conditions preceding potential habitability. Interestingly, as shown in Fig. 1, an Earth-like planet with a similar equilibrium temperature, as we used in our simulations, orbiting a star younger than our reference star AU Mic would enter the habitable zone as the star settles onto the main sequence. Therefore, if we hypothesize that these atmospheres adequately represent systems at an early evolutionary stage, our simulations with varying water content can be linked to the potential future presence of liquid water reservoirs on the planetary surface, once conditions become favourable for water condensation. For example, in Paper II, we found that flares in cooler M dwarfs with longer evolution timescales, such as Karmn J07446+035 (YZ CMi, spectral type M4.5), are well represented by the YMDF model. Further research is required to evaluate whether the YMDF model accurately captures the flare characteristics of young M dwarfs.

The chemical behaviour observed across the atmospheric grid can be understood in terms of several dominant photochemical processes. In all cases, photolysis of H_2O in the upper atmosphere provides the primary source of H, O, and OH radicals under both quiescent and flaring conditions. The subsequent fate of oxygen is governed by the local redox environment: in hydrogen-rich upper atmospheres, O and O_2 are efficiently recycled back into reduced species through reactions with H and H_2, suppressing long-term oxygen accumulation, whereas in compositions where hydrogen is less abundant or more readily lost, recombination pathways allow O and O_2 to persist. Carbon-bearing species respond primarily to enhanced UV-driven destruction during flare events, with CH_4 being particularly susceptible owing to its rapid photolysis, while CO and CO_2 are comparatively more stable and can be replenished from deeper layers through vertical mixing. The interplay between these competing processes, namely photolysis, radical recycling, and vertical transport, governs the time-dependent composition of the upper atmosphere and accounts for the contrasting chemical outcomes observed across the different flare scenarios.

Throughout the atmospheric grid, certain species, both inert, such as helium, and reactive, like water vapour, maintain consistent mixing ratios across all pressure layers, except in the uppermost layer, where even in the CF model, stellar radiation is sufficient to deplete these species. Conversely, other species become increasingly responsive to flare activity in the hydrogen-dominated atmospheres. This effect is most pronounced in the YMDF model, but nearly absent in the FF and FF400K model.

Numerous complex interactions occur in the lower atmosphere; for instance, redox reactions between a hot silicate surface and a steam-rich atmosphere can profoundly influence the oxidation states of both the surface and atmospheric species. Oxygen radicals generated from water vapour tend to oxidize surface minerals, altering their chemistry, while reducing agents such as H_2 and CO drive the reduction of metal oxides, fostering intricate chemical cycles at this interface. These processes critically modulate atmospheric composition and surface mineralogy, impacting volatile cycling and planetary habitability (Fegley et al. 2020; Zahnle et al. 2020; Hu et al. 2012). Additionally, the present simulations employ a simplified N-C-H-O chemical network, excluding metal-bearing and sulphur-containing species (e.g., SiO, Na, K, FeO, sulphur compounds). These are vital for understanding processes in the secondary planetary atmospheres (Guimond et al. 2023), which are theorized as the next stage in the evolution of terrestrial planet atmospheres after the primordial phase we focused on in this study. Our simulation setup does not fully incorporate processes related to surface–atmosphere exchange and lower atmospheric chemistry, which introduces inherent limitations to interpreting the results.

The simulations within the atmospheric grid suggest a distinct discontinuity between the upper and lower atmospheric layers, resulting in their chemical and physical responses being partially decoupled. Similar findings were reported in Louca et al. 2023; Gibbs & Fitzgerald 2025; Konings et al. 2022; Nicholls et al. 2023. Stellar radiation, particularly the UV flux from flares, predominantly affects the upper layers, with species of low mixing ratios showing signs of this impact extending deeper. Although our simulations are parametrised for H_2–H_2O-dominated atmospheres, several of the controlling mechanisms are expected to be generic. The depth of perturbation is set by UV and self-shielding, while long-term evolution depends on the balance between radical production, chemical recycling, and vertical transport. Quantitative results will differ for other compositions, but the dependence on flare statistics and shielding efficiency should hold broadly.

Louca et al. (2023) similarly employed VULCAN with a stochastic flaring routine on M-dwarf exoplanet atmospheres, finding gradual accumulation of chemical perturbations in

species such as H, OH, and CH_4 in hydrogen- or nitrogen-dominated atmospheres of similar T_{eq}, consistent with our result that trace species at low mixing ratios are most susceptible to flare-driven changes under the YMDF model. Konings et al. (2022) found that high-energy flares permanently modify upper atmospheric composition in a tidally locked gas giant using a pseudo-2D framework; whilst their target differs substantially from our water-rich primordial grid of terrestrial planets, the persistent upper-atmospheric perturbations are likely analogous, and a similar upper and lower atmosphere decoupling was recovered. Nicholls et al. (2023) also demonstrated that temperature–chemistry feedback plays an important role in determining long-term atmospheric evolution under flares, particularly for cooler planets, with the UV radiation is absorbed at lower pressures in planets with similar T_{eq} to our setup compared to the hotter planets.

Comparing models with and without interior heating within our grid, such as FF and FF400K, the layering becomes more evident: the additional heating primarily alters chemistry in the lower layers without significant upward propagation. Similarly, whilst the YMDF model produces long-term changes in the upper atmosphere, the YMDF400K setup confines the effect on mixing ratios predominantly to the lower atmosphere. This could indicate that processes not explicitly accounted for in the model, such as surface redox chemistry or outgassing, exert minimal influence on the upper atmospheric composition, particularly in hydrogen-dominated primordial atmospheres with solar elemental abundances. Consequently, the apparent decoupling between upper and lower atmospheric chemical regimes remains a robust feature within the framework of the current model assumptions.

Our results further indicate that flare activity does not contribute significantly to heating the upper atmospheric layers; instead, photochemistry plays the dominant role. This is consistent with Gibbs & Fitzgerald (2025), who demonstrate, using a brown dwarf as a hydrogen-rich analogue, that a clear discontinuity between upper and lower atmospheric regions persists and that despite significant photochemical effects the thermal influence of even the most energetic flares remains minimal, hereby hinting on the applicability of our approach with our T-P profile is held fixed, following the negligible thermal response to UV irradiation shown in Section 3.3. However, self-consistent feedback across our diverse composition grid remains an avenue for future work.

Finally, Chen et al. (2021) used a 3D coupled chemistry–climate model to show that recurring flares drive rocky planet atmospheres in older M dwarf systems into persistent chemical disequilibrium, with flare-driven signatures of bio-indicating species potentially detectable with future instruments; Chen et al. (2025) further showed, using a 3D general circulation model with interactive photochemistry, that cumulative flare effects are largely determined by flare frequency whilst instantaneous effects depend on spectral shape and energy, consistent with the contrasting behaviours we observe between the YMDF and FF models. Our results extend this picture to a broader primordial composition space, though their 3D framework captures dynamical effects beyond our current 1D treatment, motivating future extensions of this work.

4.2. FFDs may shape primordial upper atmospheres of early exo-Earths

The largest flare simulated in the YMDF model exhibits a bolometric energy approximately 6.2 times greater and a TESS band energy about 5.5 times greater than the corresponding flare in the FF model. The larger flare amplitude simulated in the YMDF compared to the FF model can be attributed to limitations in the model flare spectrum, as detailed in Paper II (see, e.g., Figure 3, right inset, specifically for 6000-7000 Å spectral range). These limitations stem from the FF model's approach to handling an incomplete observed panchromatic spectrum combined with a simplified box-car temporal flare evolution. It should be noted that such deficiencies are inherent wherever observational coverage of the full spectral range is lacking. The FF model fundamentally relies on observed panchromatic fluxes as input, and any gaps or limitations in this observational dataset can introduce uncertainness in the simulated flux density at specific temporal points during the flare event, thereby affecting the accuracy of the integrated flare energy in the simulation. Throughout the atmospheric grid in this study, the FF model effectively induces flare-related changes confined to much shallower layers in the upper atmosphere compared to the YMDF model. The deficiency in flare energies simulated in the FF model limits its capacity to produce significant atmospheric changes, whereas the variable flare energies in the YMDF model enable changes that may persist over longer timescales. It remains plausible that if the FF model adequately captured these higher-energy flares, it could similarly drive such persistent atmospheric modifications.

In this work, we studied the atmospheric scenarios and found that the FFDs used in atmospheric modelling affect the mixing ratios of species in primordial early exo-Earth atmospheres around M dwarfs. The YMDF model applies a broken power-law FFD, representing flare behaviour typical of younger M dwarfs as established in Paper I, while the FF model uses a single power-law FFD based on the observations of older M dwarf population (Loyd et al. 2018). Under similar assumption about planet-star geometry, planetary parameters and atmospheric conditions, the YMDF and FF stellar flare forcing lead to distinct atmospheric responses. The flare energy distribution critically governs the photochemical evolution of the upper atmosphere. Frequent low-energy flares efficiently deplete the limited H_2O reservoir in the tenuous, radiation-dominated upper layers, driving the local chemistry toward an H-rich, O-poor state; once this shallow layer is cleared of water, subsequent small flares contribute little additional photodissociation, while oxygen-bearing photoproducts are redistributed to deeper layers where recombination is more effective. By contrast, less frequent but more energetic flares penetrate deeper into the atmosphere, probe larger water reservoirs, and sustain photodissociation over a broader altitude range, maintaining a non-negligible population of oxygen-bearing species and preserving a more balanced local H/O chemistry. These results imply that it is the shape of the flare energy distribution, rather than the time-averaged high-energy flux alone, that determines whether water-rich upper atmospheres evolve toward transient H-dominated layers or retain observable oxygen signatures at altitudes accessible to future transmission spectroscopy.

The accumulation of O_2 to substantial levels in some of our simulations (up to 10% in the 100% water-vapour-dominated configuration) raises the question of biosignature false positives (Meadows et al. 2018). However, the planetary configurations considered in this study are not amenable to atmospheric characterisation with James Webb Space Telescope (JWST, Gardner et al. 2006) and ESA's Ariel (Tinetti et al. 2018) missions, which are both targeted to detect spectral features in larger planets at these orbital separations. Future facilities will, however, be capable of addressing this directly. The Habitable World Ob-

servatory (HWO)[7] will achieve $R \sim 150$ visible resolution at 10-pc distances, enabling simultaneous O_2/O_4 collision-induced absorption observations at 0.34–0.7 μm. LIFE[8], a proposed mid-infrared nulling interferometer array, will characterise thermal emission ($R \sim 50$, 4–18.5 μm) from nearby temperate terrestrial planets, with co-detection of O_3 (9.6 μm) and CH_4 (7.7 μm) as biosignatures.

The FF and YMDF flare frequency distributions, therefore, produce markedly divergent upper atmospheric compositions with potential implication for the future observations. The divergence originates in how each FFD shapes the time-dependent energy input, governing both the production rates of reactive species (see Appendix A.3) and their vertical transport throughout the atmospheric column. These differences propagate into substantially distinct chemical compositions and structural profiles in the upper atmosphere, with potential consequences for long-term atmospheric evolution. For photochemical studies of young M-dwarf systems, the YMDF model is the more physically motivated choice: the contrast with the FF model is sufficiently pronounced that adopting the latter would risk substantially underestimating flare-driven perturbations in the primordial regime most relevant to early atmospheric evolution. The YMDF framework therefore provides a stronger basis for interpreting future observational data and for exploring how stellar flaring shapes the evolutionary pathways of terrestrial exoplanet atmospheres.

4.3. Atmospheric escape and volatile retention

Using our modelling approach, we can probe young M dwarf planets by simulating the evolution of their atmospheric compositions and potentially predicting the fate of water within explored parameter space. In Fig. 10, we presented the diffusion-limited escape flux averaged over one year for the main atmospheric species. It is important to emphasise that these values represent not the actual escape rates but rather quantify the diffusion-limited supply of species below the exobase, which marks the altitude where escape processes may operate.

Atmospheric escape processes can be categorised into thermal escape, controlled by stellar radiation including X-UV, EUV, and IR fluxes (accounted for in this study), and non-thermal escape mechanisms, driven by the complex interplay between the stellar wind and the planetary atmosphere, including magnetic field interactions (for a comprehensive review on atmospheric escape, see Hazra 2025). These processes are inherently a three-dimensional phenomenon influenced by complex processes such as day-night temperature asymmetries, planetary magnetic fields, and spatial variations in stellar irradiation. 1D modelling, while simplify many of these features, have proven to be extremely valuable for long-term planetary evolution studies where computational efficiency and parameter exploration are essential and capture the fundamental physics governing mass-loss rates and upper atmospheric structure while enabling systematic investigations across a broad parameter space (Kubyshkina et al. 2018; Johnstone et al. 2018; Allan & Vidotto 2019). Therefore, utilising 1D kinetic chemistry models can be beneficial, but it is essential to couple them with advanced atmospheric escape modelling approaches to comprehensively account for multiple loss processes.

In this study, we calculated the diffusion-limited escape rates at the exobase of the similar atmospheres to Yoshida et al. (2022). They showed that H_2O vapour and photochemical products enhance radiative cooling in hydrodynamic outflows around M-dwarf HZ terrestrial exobase, reducing H escape by ten times at basal H_2O/H_2=0.1, potentially preserving H_2/H_2O beyond the pre-main-sequence runaway greenhouse phase. Coupling diffusion-limited escape calculations that incorporate that incorporate modelled stellar variability in young stars with hydrodynamic escape simulations above the exobase would be a natural next step toward a more comprehensive model of atmospheric loss.

Our results suggest that water is remarkably persistent: mixing ratios remain stable throughout the atmospheric column below the exobase over the full one-year span of our simulations, with the exception of the uppermost layers. Water self-shields against photodissociation, allowing volatile retention over long timescales even under active flaring conditions. This has direct implications for volatile retention and long-term habitability potential on planets orbiting M dwarfs, hinting at a potentially available water reservoir should conditions on the planet become habitable, as illustrated in Figure 1.

By understanding the evolutionary pathways in these primordial atmospheres with varying water content, we can predict the observational signatures expected in systems evolving toward habitable planets. However, to achieve this, it is necessary to improve our model by incorporating additional atmospheric escape processes beyond the current state-of-the-art, thereby providing a more comprehensive account of water loss mechanisms and planetary evolution.

5. Conclusion

We explored the parameter space of atmospheric chemical kinetics in primordial (0.1-100%H_2O) atmospheres of early exo-Earth, orbiting active M dwarfs. Due to observational challenges, empirical constraints on stellar activity remain limited, which motivated the development of the Young M dwarf flare model capable of producing temporally resolved flare fluxes. Given that M dwarf activity predominantly occurs in the UV range, our simulations provide predictions for the potential development of liquid water reservoirs on planets as their host stars evolve toward the main sequence. Flare activity primarily affects atmospheric chemistry in the upper layers, while the lower atmosphere appear decoupled from the photochemistry driven upper envelopes. These findings therefore provide a framework applicable beyond the specific atmospheric regime modelled, with flare statistics and shielding efficiency acting as key controls on chemical evolution in terrestrial atmospheres more generally.

Flare frequency distributions play a role in shaping upper atmospheric chemistry, with the YMDF model capturing high-energy and mid-size flares that induce deeper and potentially persistent atmospheric changes compared to the 'fiducial flare' model. Our diffusion-limited escape calculations at the exobase provide important constraints on an atmospheric species transport, establishing a lower bound on atmospheric loss under hydrodynamic escape conditions. Future work should couple diffusion-limited escape calculations that incorporate stellar variability with hydrodynamic simulations including radiative cooling, thereby developing integrated atmospheric escape models.

It is essential to understand water loss and atmospheric evolution during the prolonged runaway greenhouse phase. The long-term retention of water below the exobase, sustained by photochemical self-shielding and robust against active flaring, implies that a significant volatile reservoir may persist on such

[7] https://habitableworldsobservatory.org/home
[8] https://life-space-mission.com/

worlds, with direct consequences for habitability assessments of M-dwarf exoplanet systems. Exploring the observational detectability of the predicted atmospheric signatures presents a promising future direction and warrants dedicated investigation in subsequent analyses. Future facilities such as HWO and LIFE will enable discrimination of the abiotic O_2 accumulation identified here from biologically sustained disequilibria, through co-detection of complementary biosignature tracers. Addressing the gaps in current modelling approaches will enhance our predictive capabilities regarding atmospheric composition evolution, planetary habitability, and observational signatures in young, active M dwarf exoplanet systems.

Acknowledgements. We acknowledge financial support from the Research Council of Norway (RCN), through its Centres of Excellence funding scheme, projects number 332523 (PHAB, Centre for Planetary Habitability) and number 262622 (RoCS, Rosseland Centre for Solar Physics). We thank an anonymous referee for helpful comments and critiques, which have significantly improved the quality of this manuscript.

References

Airapetian, V. S., Glocer, A., Khazanov, G. V., et al. 2017, ApJ, 836, L3
Allan, A. & Vidotto, A. A. 2019, MNRAS, 490, 3760
Andersen, J. M. & Korhonen, H. 2015, MNRAS, 448, 3053
Berger, V. L., Hinkle, J. T., Tucker, M. A., et al. 2024, MNRAS, 532, 4436
Borucki, W. J., Koch, D., Basri, G., et al. 2010, Science, 327, 977
Borysow, A. 2002, A&A, 390, 779
Brasseur, C. E., Osten, R. A., Tristan, I. I., & Kowalski, A. F. 2023, ApJ, 944, 5
Brown, A., Schneider, P. C., France, K., et al. 2023, AJ, 165, 195
Chen, H., De Luca, P., Hochman, A., & Komacek, T. D. 2025, AJ, 170, 40
Chen, H., Zhan, Z., Youngblood, A., et al. 2021, Nature Astronomy, 5, 298
Crossfield, I. J. M. & Kreidberg, L. 2017, AJ, 154, 261
Davenport, J. R. A. 2016, ApJ, 829, 23
Davenport, J. R. A., Hawley, S. L., Hebb, L., et al. 2014, ApJ, 797, 122
Dotter, A. 2016, ApJS, 222, 8
Dressing, C. D. & Charbonneau, D. 2015, ApJ, 807, 45
Fegley, Jr., B., Lodders, K., & Jacobson, N. S. 2020, Chemie der Erde / Geochemistry, 80, 125594
Feinstein, A. D., France, K., Youngblood, A., et al. 2022, AJ, 164, 110
Feinstein, A. D., Seligman, D. Z., France, K., Gagné, J., & Kowalski, A. 2024, AJ, 168, 60
France, K., Duvvuri, G., Egan, H., et al. 2020, AJ, 160, 237
France, K., Loyd, R. O. P., Youngblood, A., et al. 2016, ApJ, 820, 89
Froning, C. S., Kowalski, A., France, K., et al. 2019, ApJ, 871, L26
Gaia Collaboration. 2020, VizieR Online Data Catalog: Gaia EDR3 (Gaia Collaboration, 2020), VizieR On-line Data Catalog: I/350. Originally published in: 2021A&A...649A...1G
Gaidos, E. & Mann, A. W. 2013, ApJ, 762, 41
Gardner, J. P., Mather, J. C., Clampin, M., et al. 2006, Space Sci. Rev., 123, 485
Garraffo, C., Alvarado-Gómez, J. D., Cohen, O., & Drake, J. J. 2022, ApJ, 941, L8
Garraffo, C., Drake, J. J., Cohen, O., Alvarado-Gómez, J. D., & Moschou, S. P. 2017, ApJ, 843, L33
Gershberg, R. E. 1972, Ap&SS, 19, 75
Gibbs, A. & Fitzgerald, M. P. 2025, ApJ, 993, 41
Green, J. C., Froning, C. S., Osterman, S., et al. 2012, ApJ, 744, 60
Guimond, C. M., Shorttle, O., Jordan, S., & Rudge, J. F. 2023, MNRAS, 525, 3703
Hawley, S. L., Davenport, J. R. A., Kowalski, A. F., et al. 2014, ApJ, 797, 121
Hazra, G. 2025, Reviews of Modern Plasma Physics, 9, 18
Howard, W. S., Corbett, H., Law, N. M., et al. 2019, ApJ, 881, 9
Howell, S. B., Sobeck, C., Haas, M., et al. 2014, PASP, 126, 398
Hu, R., Seager, S., & Bains, W. 2012, ApJ, 761, 166
Jackman, J. A. G., Shkolnik, E. L., Loyd, R. O. P., & Richey-Yowell, T. 2024, MNRAS, 533, 1894
Johnstone, C. P., Güdel, M., Lammer, H., & Kislyakova, K. G. 2018, A&A, 617, A107
Kalirai, J. 2018, Contemporary Physics, 59, 251
Katyal, N., Ortenzi, G., Lee Grenfell, J., et al. 2020, A&A, 643, A81
Kempton, E. M. R., Lessard, M., Malik, M., et al. 2023, ApJ, 953, 57
Konings, T., Baeyens, R., & Decin, L. 2022, A&A, 667, A15
Kopparapu, R. K., Ramirez, R. M., SchottelKotte, J., et al. 2014, ApJ, 787, L29
Kowalski, A. F., Wisniewski, J. P., Hawley, S. L., et al. 2019, ApJ, 871, 167
Kubyshkina, D., Fossati, L., Erkaev, N. V., et al. 2018, ApJ, 866, L18
Kulikov, Y. N., Lammer, H., Lichtenegger, H. I. M., et al. 2006, Planet. Space Sci., 54, 1425
Kuramoto, K., Umemoto, T., & Ishiwatari, M. 2013, Earth and Planetary Science Letters, 375, 312
Lissauer, J. J., Fabrycky, D. C., Ford, E. B., et al. 2011, Nature, 470, 53
Louca, A. J., Miguel, Y., Tsai, S.-M., et al. 2023, MNRAS, 521, 3333
Loyd, R. O. P. 2022, fiducial_flare: Spectra and lightcurves of a standardized far ultraviolet flare, Astrophysics Source Code Library, record ascl:2202.012
Loyd, R. O. P., France, K., Youngblood, A., et al. 2018, ApJ, 867, 71
Luger, R. & Barnes, R. 2015, Astrobiology, 15, 119
Malik, M., Grosheintz, L., Mendonça, J. M., et al. 2017, AJ, 153, 56
Malik, M., Kempton, E. M. R., Koll, D. D. B., et al. 2019, ApJ, 886, 142
Mamonova, E., Kowalski, A. F., Herbst, K., Wedemeyer, S., & Werner, S. C. 2026, A&A, 705, A165
Mamonova, E., Shan, Y., Kowalski, A. F., Wedemeyer, S., & Werner, S. C. 2025, A&A, 700, A53
Meadows, V. S., Reinhard, C. T., Arney, G. N., et al. 2018, Astrobiology, 18, 630
Miguel, Y., Kaltenegger, L., Linsky, J. L., & Rugheimer, S. 2015, MNRAS, 446, 345
Miller-Ricci Kempton, E., Zahnle, K., & Fortney, J. J. 2012, ApJ, 745, 3
Modi, A., Estrela, R., & Valio, A. 2023, MNRAS, 525, 5168
Moses, J. I., Bézard, B., Lellouch, E., et al. 2000, Icarus, 143, 244
Moses, J. I., Line, M. R., Visscher, C., et al. 2013, ApJ, 777, 34
Moses, J. I., Tremblin, P., Venot, O., & Miguel, Y. 2022, Experimental Astronomy, 53, 279
Newton, E. R., Irwin, J., Charbonneau, D., Berta-Thompson, Z. K., & Dittmann, J. A. 2016, ApJ, 821, L19
Nicholls, H., Hébrard, E., Venot, O., Drummond, B., & Evans, E. 2023, MNRAS, 523, 5681
Owen, J. E., Shaikhislamov, I. F., Lammer, H., Fossati, L., & Khodachenko, M. L. 2020, Space Sci. Rev., 216, 129
Owen, T. 1980, in Strategies for the Search for Life in the Universe: A Joint Session of Commissions 16, 40, and 44, Held in Montreal, Canada, During the IAU General Assembly, 15 and 16 August, 1979, ed. M. D. Papagiannis (Dordrecht: Springer Netherlands), 177–185
Padovani, P. & Cirasuolo, M. 2023, Contemporary Physics, 64, 47
Parmentier, V., Showman, A. P., & Lian, Y. 2013, A&A, 558, A91
Paudel, R. R., Barclay, T., Youngblood, A., et al. 2024, ApJ, 971, 24
Paxton, B., Smolec, R., Schwab, J., et al. 2019, ApJS, 243, 10
Ranjan, S., Wordsworth, R., & Sasselov, D. D. 2017, ApJ, 843, 110
Rauer, H., Aerts, C., Cabrera, J., et al. 2025, Experimental Astronomy, 59, 26
Ribas, I., Bolmont, E., Selsis, F., et al. 2016, A&A, 596, A111
Richard, C., Gordon, I. E., Rothman, L. S., et al. 2012, J. Quant. Spec. Radiat. Transf., 113, 1276
Ricker, G. R. 2016, in AGU Fall Meeting Abstracts, P13C–01
Ricker, G. R., Winn, J. N., Vanderspek, R., et al. 2015, Journal of Astronomical Telescopes, Instruments, and Systems, 1, 014003
Ridgway, R. J., Zamyatina, M., Mayne, N. J., et al. 2023, MNRAS, 518, 2472
Scalo, J., Kaltenegger, L., Segura, A., et al. 2007, Astrobiology, 7, 85
Segura, A., Walkowicz, L. M., Meadows, V., Kasting, J., & Hawley, S. 2010, Astrobiology, 10, 751
Sneep, M. & Ubachs, W. 2005, J. Quant. Spec. Radiat. Transf., 92, 293
Stock, J. W., Kitzmann, D., Patzer, A. B. C., & Sedlmayr, E. 2018, MNRAS, 479, 865
Tilley, M. A., Segura, A., Meadows, V., Hawley, S., & Davenport, J. 2019, Astrobiology, 19, 64
Tinetti, G., Drossart, P., Eccleston, P., et al. 2018, Experimental Astronomy, 46, 135
Tovar Mendoza, G., Davenport, J. R. A., Agol, E., Jackman, J. A. G., & Hawley, S. L. 2022, AJ, 164, 17
Tsai, S.-M., Lyons, J. R., Grosheintz, L., et al. 2017, ApJS, 228, 20
Tsai, S.-M., Malik, M., Kitzmann, D., et al. 2021, ApJ, 923, 264
Tsai, S.-M., Steinrueck, M., Parmentier, V., Lewis, N., & Pierrehumbert, R. 2023, MNRAS, 520, 3867
Wittrock, J. M., Plavchan, P. P., Cale, B. L., et al. 2023, AJ, 166, 232
Yoshida, T., Terada, N., Ikoma, M., & Kuramoto, K. 2022, ApJ, 934, 137
Zahnle, K. J. & Catling, D. C. 2017, ApJ, 843, 122
Zahnle, K. J., Lupu, R., Catling, D. C., & Wogan, N. 2020, Planet. Sci. J., 1, 11

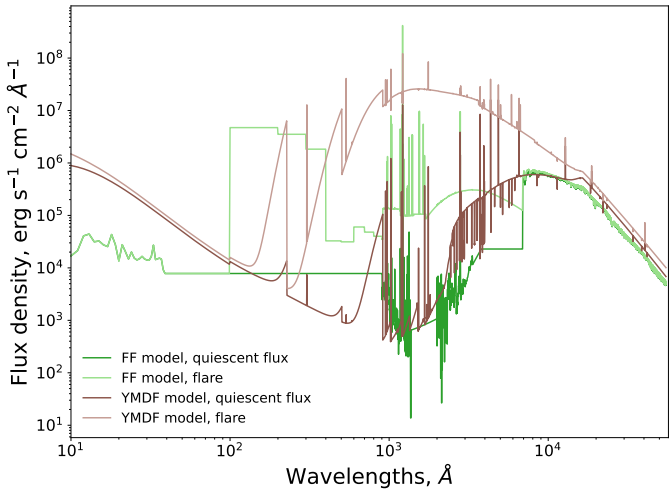

Fig. A.1. Flux densities for the FF and YMDF models: quiescent and averaged over the duration of the largest synthetic flare in the respective datasets. Fluxes are shown for the quiescent state (solid brown and green lines for the YMDF and FF models, respectively) and flare-averaged state (solid light-brown and light-green lines for the YMDF and FF models, respectively). The YMDF model exhibits a clear excess in UV and NUV flux density during its largest recorded flare in the dataset compared to the largest recorded flare in the FF model, whilst at wavelengths beyond ~ 3200 Å both models show good agreement with each other and only a marginal excess above the respective quiescent stellar continuum.

Appendix A: Modelling approach limitations

Appendix A.1: Helios T-P profiles and 1D atmospheric models

While HELIOS generates reliable atmospheric profiles under radiative equilibrium and offers flexibility in input chemistry and stellar parameters, the code is subject to several limitations. The 1D framework neglects horizontal inhomogeneities and atmospheric circulation that can affect thermal structures. Our interpretation also excludes cloud formation, the time-dependent stellar variability is not yet realised in HELIOS, and the computations consider equilibrium chemistry, limiting the code application in atmospheres dominated by dynamic or transient stellar phenomena.

Following Malik et al. (2019), who use ideal gas approximations, Kempton et al. (2023) propose an alternative method deriving adiabatic coefficients and specific heat capacities from gas entropy accounting for local chemical composition. Their T-P profiles for planets with Earth-like gravity and 500 K equilibrium temperature align closely with ours near the upper atmosphere, despite differences at higher pressures due to structural assumptions (with or without surface, the former assumption is adopted in this study, see Fig. 5, right panel in Sect. 3.3).

Appendix A.2: YMDF and FF models during the largest flares in the dataset

Figure A.1 shows the flux density spectra of the YMDF and FF stellar models in both quiescent and flare states. The spectra of the largest synthetic flares in the YMDF and FF datasets (see the flare data stated in Sect. 3.2) are plotted as the average flux density over the duration of the flare. In the EUV band, the FF flare is represented as a coarse histogram due to missing spectral data in this range in the panchromatic quiescent spectra from Feinstein et al. (2022), and this effect is described in Paper II. The YMDF flare therefore shows smaller flux values compared to the FF model. This spectral region is important for the photodissociation of molecules such as H_2O and CO_2, and both models suffer from a lack of observational data that could help better characterise this regime. In the FUV, both flare spectra are highly structured owing to Lyman-series absorption and emission features. However, the most energetic flare in the FF model is a factor of ~ 10^2 lower than the YMDF model across this region. The Lyman-α line appears as a sharp absorption trough in both models, though the associated line emission flanking it is considerably more pronounced in YMDF. In the NUV, the YMDF flare remains elevated, declining only gradually toward longer wavelengths. The FF flare rises modestly in this window, with the YMDF excess over FF somewhat smaller than in the FUV. This region overlaps strongly with the photolysis cross-sections of photochemically active species, making the flux discrepancy between the two models particularly consequential for photochemical modelling. Beyond ~ 3200 Å, the two flare spectra converge toward their respective quiescent spectra, both following the photospheric continuum into the infrared.

Appendix A.3: Rate coefficients' evolution induced by flares

We introduced variable stellar flux to the atmospheres, where calculates chemical kinetic evolution of species, and these changes directly affect the rate coefficients $J_s(z)$, which govern the photodissociation of each chemical species s at altitude z. The rate coefficient is computed as

$$J_s(z) = \int_\lambda \Phi(z,\lambda)\,\sigma_s(\lambda)\,\mathrm{d}\lambda, \tag{A.1}$$

where $\Phi(z,\lambda)$ is the actinic flux, representing the total photon flux integrated over all directions available to a molecule at altitude z and wavelength λ, and $\sigma_s(\lambda)$ is the photodissociation cross-section of species s. The actinic flux is derived from the total radiative intensity via $\Phi = F_{\mathrm{tot}}/(hc/\lambda)$, where h is the Planck constant and c is the speed of light, converting energy flux in erg s^{-1} cm^{-2} Å^{-1} into photon number flux in photons s^{-1} cm^{-2} Å^{-1}. The stellar spectrum is interpolated onto a uniform wavelength grid of 240 bins with a resolution of 0.1 nm below 240 nm and 2.0 nm above 240 nm, and the cross-sections are binned onto the same grid.

The photolysis rate coefficients were sampled several days after the largest flare in each model rather than at the moment of peak flux, as the atmospheric chemistry requires time to respond to the elevated radiation field and sampling at a later epoch reveals for how long the cumulative photochemical perturbation persists. Figure A.2 shows the resulting changes in selected photolysis rate coefficients across the atmosphere for both stellar models. The dashed lines correspond to the state of the atmosphere at the end of a 10-day integration, whilst the solid lines show the final state at 360 days. Lines with markers indicate the atmospheric state in the YMDF simulation at 260 days, following the largest flare which occurred at day 243, and in the FF simulation at 140 days, following the largest flare which occurred at day 136. The elevated photolysis rates driven by the flare flux persist differently between the two models, reflecting the spectral differences in the FUV and NUV discussed above. We note that, in the FF model, the chemical signature of the largest flare has largely dissipated by day 4, whilst in the YMDF model the flare-driven perturbation remains clearly detectable 17 days after the event, reflecting the substantially larger energy input. How-

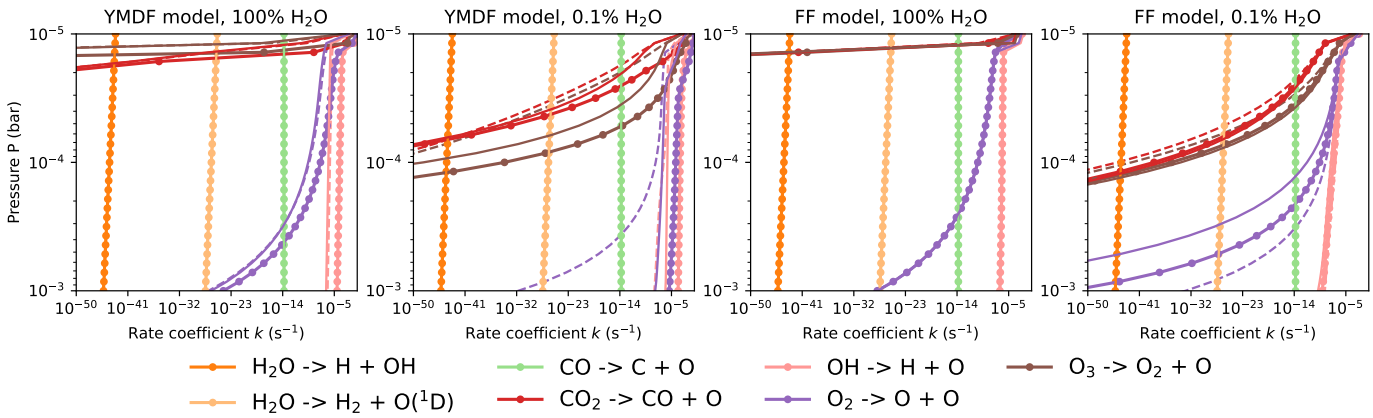

Fig. A.2. Photolysis rate coefficients $J_s(z)$ as a function of altitude for selected chemical reactions, computed in VULCAN for the YMDF and FF stellar models, and shown for the upper layers of the simulated atmospheres. Dashed lines show the atmospheric state at the end of the 10-day integration, solid lines at 360 days. In the left two panels, lines with markers correspond to the YMDF simulation at 260 days after the largest flare at day 253, and, in the two panel to the right, these lines correspond to the FF simulation at 140 days after the largest flare at day 136.

ever, examining the photolysis rates at the end of the simulations, the FF model shows that the accumulated atmospheric stress either didn't change as for H_2O photodissociation reactions or converges to values close to those observed after the largest flare in other cases, whilst in the YMDF model the substantially larger flare-driven perturbations tend to relax without departing severely from the initial values for the similar reactions. It should be emphasised that a large rate coefficient does not necessarily produce significant chemical change if the number density of the target species is low; conversely, in H_2O-rich atmospheres photodissociation proceeds efficiently even at modest rates due to the large molecular reservoir.

Appendix A.4: Thermochemical assumptions

VULCAN, like all 1D models, is inherently limited by its neglect of atmospheric dynamics, spatial heterogeneity, clouds, and surface-atmosphere interactions. Uncertainties in reaction rates and limited reaction networks constrain chemical pathway accuracy, especially under poorly explored conditions. The current version of VULCAN does not incorporate ionisation processes, which may become significant in highly irradiated or strongly ionised environments. Despite these limitations, VULCAN provides a robust and widely validated framework for probing the fundamental processes of photochemistry and thermochemistry in young, volatile-rich planetary atmospheres, as encountered around active early M dwarfs.

Appendix A.5: MLT in eddy diffusion coefficient calculation

The vertical eddy diffusion coefficient K_{zz} is parameterised using a mixing-length theory (MLT) approach, $K_{zz} = C \cdot l \cdot w_t$, where $C \sim 1$, l is a characteristic mixing length, and w_t is a turbulent velocity under the assumption of free convection. This formulation is widely used for H_2-dominated atmospheres where convection provides efficient vertical mixing over large pressure ranges (Parmentier et al. 2013; Moses et al. 2013; Miguel et al. 2015). We adopt the empirically calibrated pressure scaling from Moses et al. (2022) and Louca et al. (2023), where they assumed that the turbulent velocity is govern by stellar effective temperature, as given in Sect. 2.7, which yields K_{zz} values broadly consistent with global values can be found in the literature (10^5–10^{10}cm^{2}s^{-1}, Louca et al. 2023, their Figure 4) while allowing

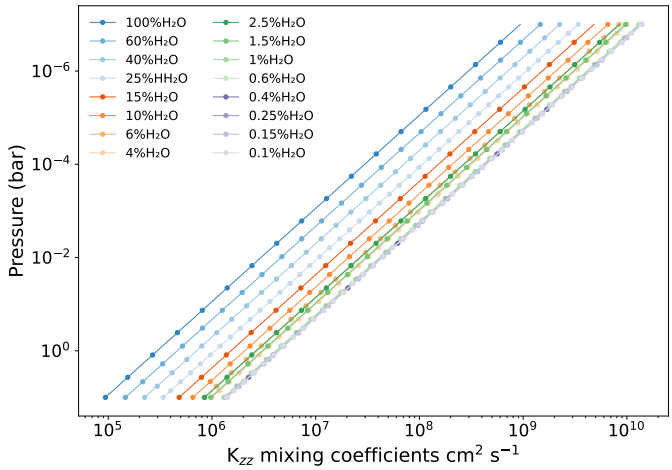

Fig. A.3. Eddy diffusion mixing coefficient (K_{zz}) profiles for the grid of the atmospheres with H_2O from 100% to 0.1%. Solid coloured lines with spheres represent K_{zz} coefficients plotted against pressure, following the colour coding indicated in the plot legend.

exploration across our atmosphere grid. Applied to rocky planets, this MLT-based prescription should be regarded as a physically motivated scaling law rather than a fully self-consistent dynamical model.

Figure A.3 shows the resulting $K_{zz}(P)$ profiles across the full atmospheric grid. profiles across the full atmospheric grid. The profiles demonstrate enhanced eddy diffusion towards lower pressures, facilitating vertical mixing of photochemically produced species throughout the atmosphere, whilst at the uppermost layers molecular diffusion takes over as the dominant transport mechanism. The profiles reflect the pressure-dependent atmospheric structure computed by HELIOS for each bulk composition from equilibrium state reached in Fastchem. For atmospheres with 10–100% H_2O, the K_{zz} profiles decrease monotonically with water abundance, as expected from the corresponding increase in mean molecular weight, which reduces the atmospheric scale height and consequently the eddy diffusion coefficient. In the intermediate range (0.6–6% H_2O), where carbon, nitrogen, and hydrogen species computed in chemical equilibrium contribute significantly to the bulk composition, the altitude-dependent pressure structure deviates from a simple

water-scaling, resulting in non-monotonic ordering of the profiles. At the lowest water abundances (0.1–0.4% H_2O), where other species dominate the composition, the K_{zz} profiles converge towards a common behaviour that is no longer sensitive to the residual water fraction. While a fully self-consistent K_{zz} derived from 3D GCMs for rocky planets around active M dwarfs would be ideal, our MLT parameterisation provides a physically motivated baseline for the present study.

Appendix A.6: Molecular diffusion parameters

In VULCAN, at the atmospheric boundaries, the discretized molecular diffusion coefficients D_{zz} incorporate molecular diffusion, gravitational settling, and thermal diffusion. The thermal diffusion factor α scales the effect of temperature gradients on species transport, dominating only near the boundaries where vertical fluxes are constrained.

In hydrogen-dominated atmospheres (H_2O <40%), particularly in the extended and low-density upper layers, molecular diffusion processes are significantly influenced by thermal diffusion factors, α, that vary according to species. In our setup, for atomic hydrogen, α was set to -0.1. It reflects a slight tendency of this light species to migrate upward along temperature gradients, enhancing its transport and potential escape. For H_2 α=0, as this species experiences minimal thermal diffusion effects, consistent with its intermediate mass and relatively well-mixed nature. Heavier species in this regime typically have positive α values around 0.25, which bias their diffusion toward cooler, denser atmospheric layers due to gravitational settling and reduced thermal diffusion, effectively constraining their vertical distribution.

Conversely, in water-rich atmospheres (H_2O≥40%) characterised by higher densities and more compact vertical structures, thermal diffusion factors were adjusted to reflect the stronger collisional coupling and differing transport dynamics. Light species such as H, He, and H_2, in our setup, have negative α values near -0.25, consistent with enhanced upward thermal diffusion driven by temperature gradients. Heavier molecules in this environment generally have $\alpha \approx 0$, indicating negligible thermal diffusion effects within the tightly coupled atmospheric matrix. The weighting of diffusion-related terms: molecular diffusivity, gravitational settling, and thermal diffusion, varies accordingly. Molecular diffusion coefficients D_{zz} are generally larger in low-density hydrogen atmospheres, amplifying all diffusive fluxes, while in dense water-dominated atmospheres, smaller diffusion coefficients diminish thermal and molecular diffusion contributions, with gravitational and collisional effects dominating heavier species transport.

Appendix B: Simulations in detail and additional figures

Appendix B.1: Evolution outlook: initial atmospheric states

We started all our simulations in the grid by calculating initial concentrations by variation of Fastchem code incorporated in VULCAN. As input, this version of Fastchem use T-P profiles we recalculated in HELIOS as described in Sect. 2.4. In Fig. B.1 we present these concentrations at the beginning of the simulation (t=0)) before applying the external flare forcing. The figure provides a visual framework to compare atmospheric mixing ratios of key species across simulation regimes and initial states before chemical kinetics evolve the system.

Appendix B.2: Number density profiles at the end of simulation

Figure B.2 presents the number density profiles of the key atmospheric species across the four flare models (YMDF, FF, FF400K, and CF) for the 100% and 0.1% H_2O boundary compositions. In both cases, the general decline in number densities toward lower pressures is a natural consequence of the decreasing atmospheric density with altitude and does not reflect chemical depletion for some species mentioned before as stable (i.e. H_2O, He, and N_2). In the 100% H_2O atmosphere, H_2O and H_2 dominate the column at all pressure levels across all models, with the remaining species occupying a broad but lower number density range. The most notable model-dependent differences appear in the upper atmosphere, where O_2 reaches appreciably higher number densities and atomic O is slightly more abundant in the YMDF and CF models compared to FF and FF400K, consistent with enhanced production of oxygen-bearing species driven by more energetic flare events. By contrast, H and CO number densities are elevated in the FF and FF400K models, particularly in the middle atmosphere.

In the 0.1% H_2O atmosphere, H_2O remains present throughout the column at number densities consistent with its prescribed mixing ratio, with the exception of the uppermost layers, but falls beneath the dynamical range dominated by H_2 and He. The number density profiles of the remaining species are broadly similar across models, with the notable exception of the YMDF case, where O and O_2 reach comparable number densities to one another, whereas in the other models atomic oxygen is more strongly depleted relative to O_2. This demonstrates that even in water-poor atmospheres, the flare energy distribution governs the relative abundances and vertical distribution of oxygen-bearing species.

Appendix B.3: Simulations' results: additional figures

Figure B.3 shows heatmaps of the O_2 mixing ratio over the full 360-day simulation for a solar abundance atmosphere containing 10% water vapour, for all models. A clear atmospheric response to the flare events is visible in the FF model, though it is less pronounced than the largest flare effect in YMDF, consistent with the lower FUV and NUV flux of the FF flares. Unlike the YMDF dataset, which consist one large flare event and numerous mid-size flares, the FF dataset contains multiple flares of energy comparable to its largest event, alongside a higher frequency of smaller flares. This produces a more distributed and cumulative photochemical perturbation in the FF model, where the combined effect of repeated moderate flares contributes to the long-term evolution. Disturbance of the atmospheric composition, forced by stellar activity, is visible in both the FF and YMDF panels, but not in CF model. However, the molecular oxygen mixing ratios in the uppermost layers are similar to those in YMDF model, consistent with values presented in Fig. 7.

Appendix B.4: Additional interior heating in the YMDF model

We analysed two extreme regimes in our atmospheric grid under the YMDF model flaring, simulating 100% and 0.1% H_2O with temperature-pressure profiles including T=400K interior heating (Fig. B.8). This heating increases oxygen abundances in both upper and lower layers, with species such as H and OH showing similar trends. Most species depicted in the two left square panels of Fig. B.8, representing the mixing ratios at the end of the 360-day simulation, show elevated concentra-

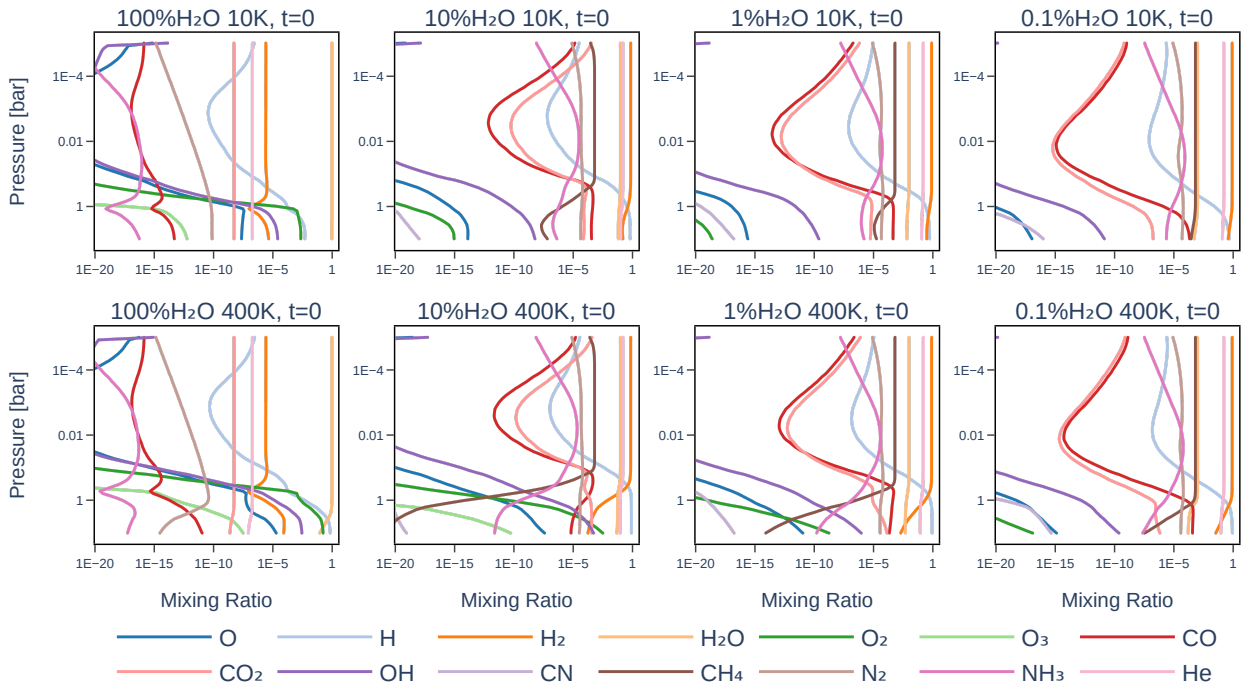

Fig. B.1. Initial atmospheric mixing ratios for four atmospheres with water fractions of 100%, 10%, 1%, and 0.1% arranged by columns, and two atmospheric regimes arranged by rows with interior heating of 10K and 400K, respectively. Concentrations are shown for the initial simulation time (t=0).

tions in the upper and lower layers, while their overall abundances in the middle of the atmosphere remain comparable to those in the YMDF model without interior heating. Species like CH_4 and NH_3 display more complex responses to the modified temperature-pressure profile. The two right horizontal panels illustrate the temporal evolution in the upper layers and show compositions similar to the YMDF model without heating, although flare responses are more smothered and prolonged.

In Fig. B.7 we present the temporal evolution of the ammonia mixing ratio for atmospheres with 100% and 0.1% H_2O fractions, comparing both the YMDF and YMDF400K models. When the H_2O abundance is low, ammonia levels gradually accumulate in the atmosphere, reaching mixing ratios of 10^{-6} and higher. These values are highly sensitive to large flares, which deplete NH_3 not only in the upper layers but also deeper within the atmosphere. Partial recovery occurs over time, yet full replenishment is not achieved within the simulation period. Introducing interior heating causes further NH_3 depletion near the atmospheric base, leading to overall lower concentrations. In water steam-dominated regimes, an initial ammonia reservoir is progressively lost through sustained stellar activity, with complete removal observed when basal heating is included.

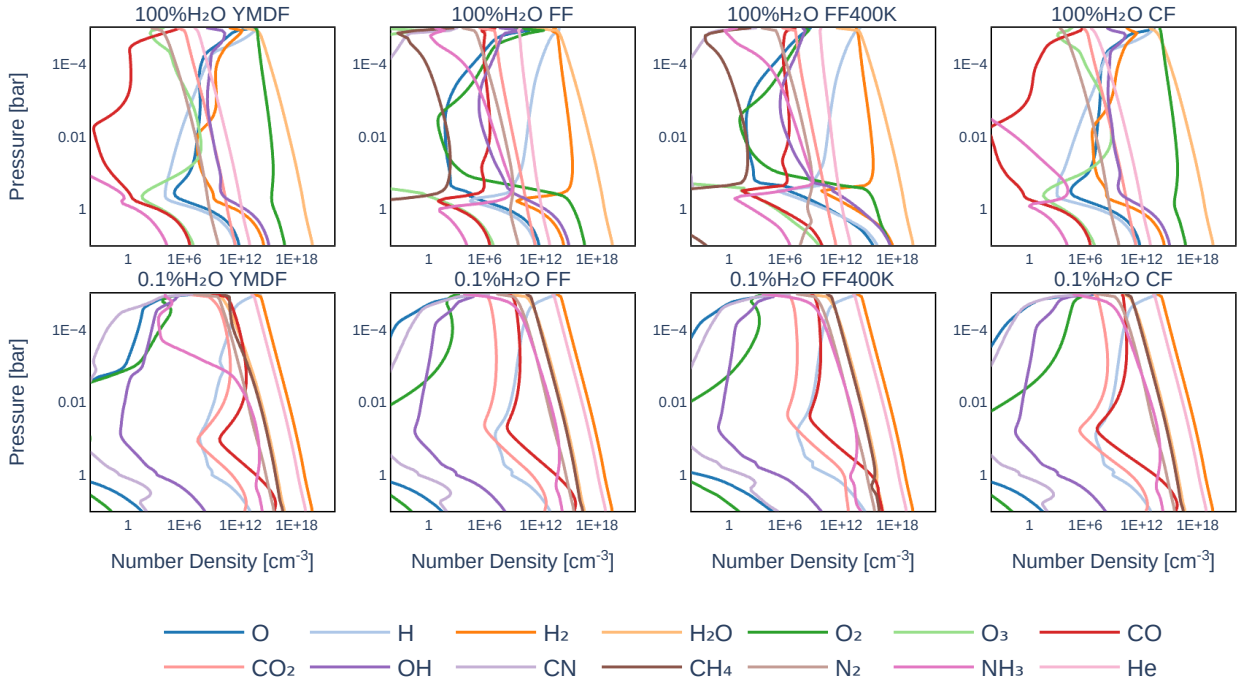

Fig. B.2. Number density profiles [cm^{-3}] as a function of pressure [bar] for key atmospheric species across the four flare models (YMDF, FF, FF400K, and CF), shown for the 100% H_2O (top row) and 0.1% H_2O (bottom row) atmospheric compositions. Species are colour-coded as indicated in the legend.

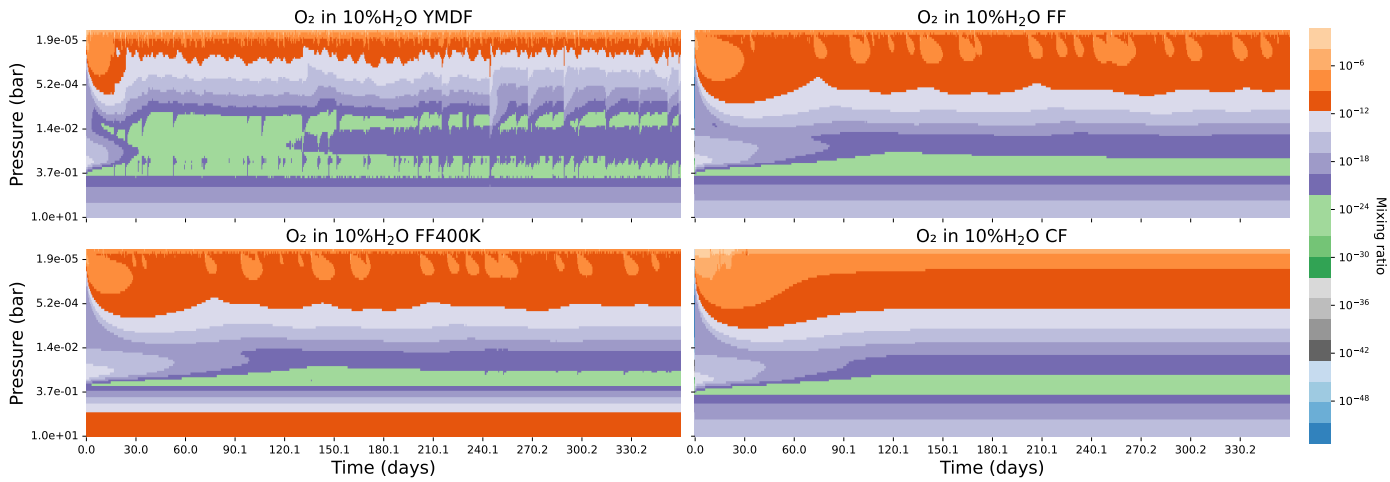

Fig. B.3. Heatmaps of O_2 mixing ratio over the 360-day simulation period for a solar abundance atmosphere containing 10% water vapour. The upper row shows results from the YMDF and FF models, while the bottom row shows the FF model heated to 400 K and the CF model, as indicated on the panels. The vertical axis represents atmospheric pressure in bars, and the horizontal axis represents simulation time in days.

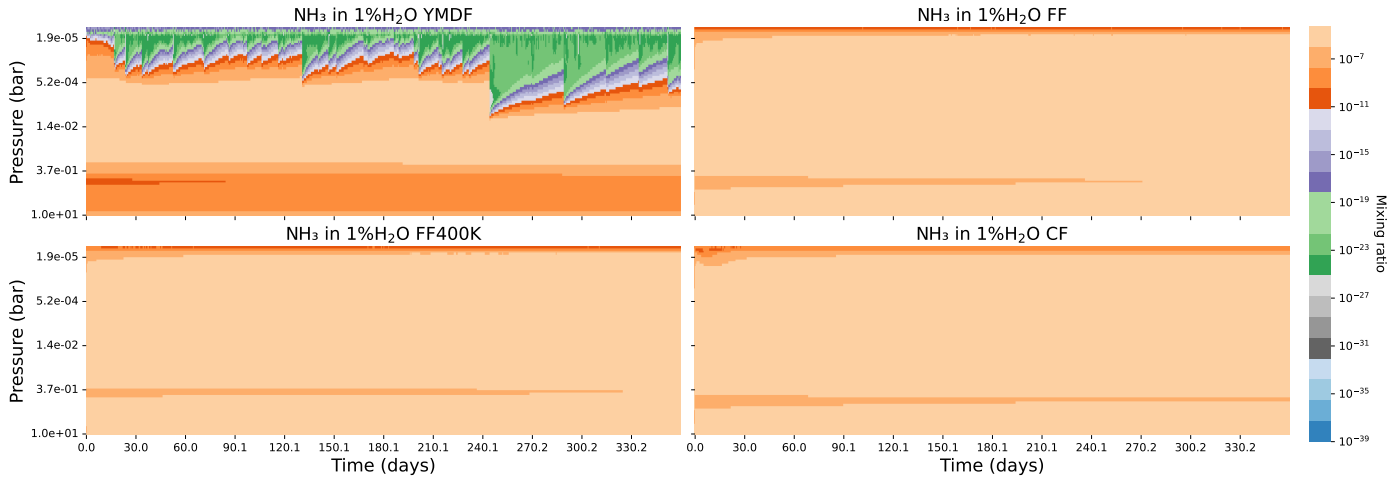

Fig. B.4. Heatmaps of NH_3 mixing ratio over the 360-day simulation period for a solar abundance atmosphere containing 1% water vapour. The upper row shows results from the YMDF and FF models, while the bottom row shows the FF model heated to 400 K and the CF model, as indicated on the panels. The vertical axis represents atmospheric pressure in bars, and the horizontal axis represents simulation time in days.

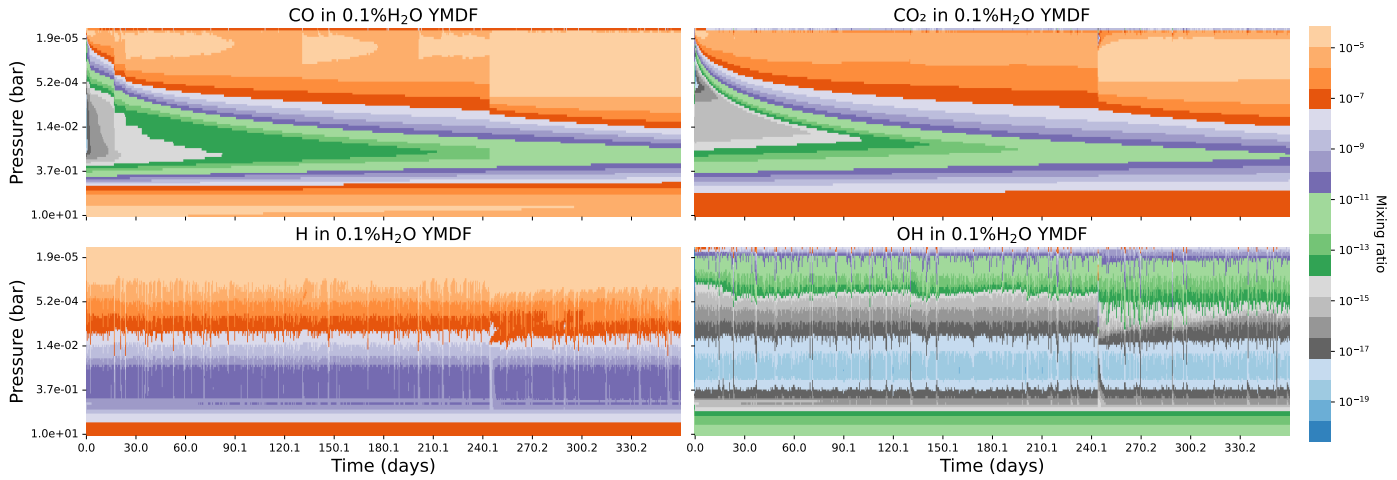

Fig. B.5. Heatmaps of CO, CO_2, H and OH mixing ratio over the 360-day simulation period for a solar abundance atmosphere containing 0.1% water vapour analogous to the previous Fig. B.4.

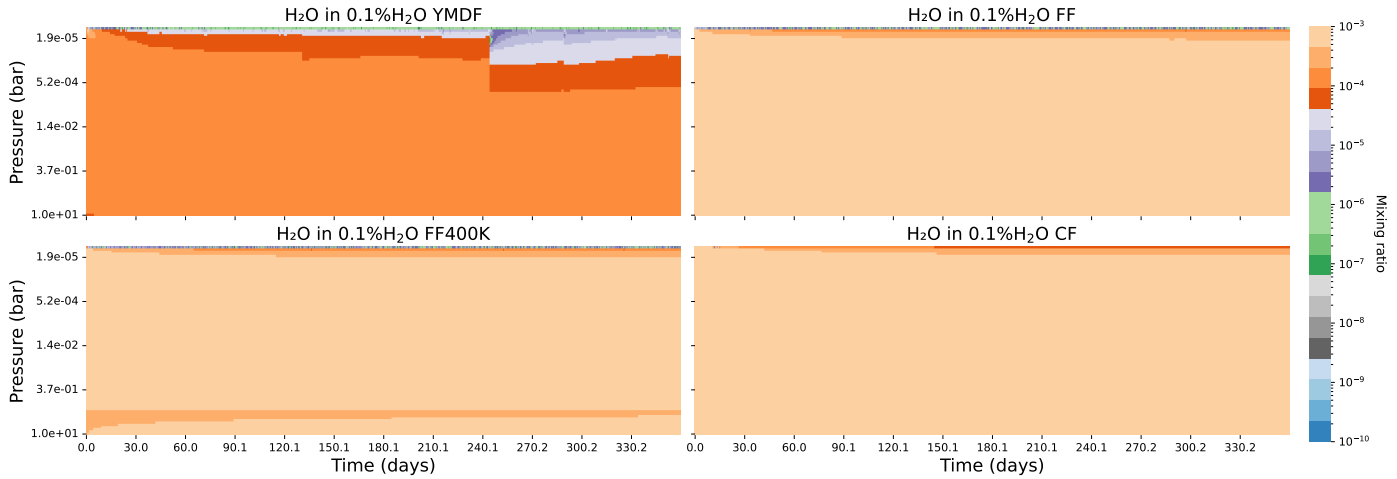

Fig. B.6. Heatmaps of H_2O mixing ratio over the 360-day simulation period for a solar abundance atmosphere containing 0.1% water vapour analogous to the previous Fig. B.4.

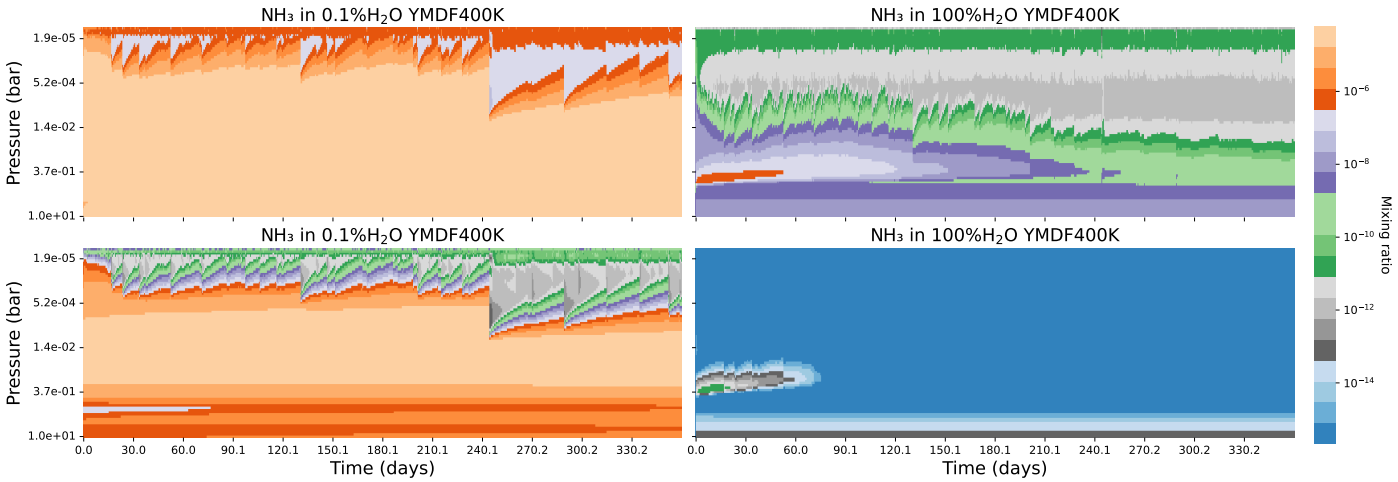

Fig. B.7. Heatmaps showing the evolution of NH_3 mixing ratios over the 360-day simulation period. The left and right panels represent atmospheres with 0.1% and 100% water vapour fractions, respectively. The top and bottom rows correspond to the YMDF model without and with interior heating (10K and 400K, respectively).

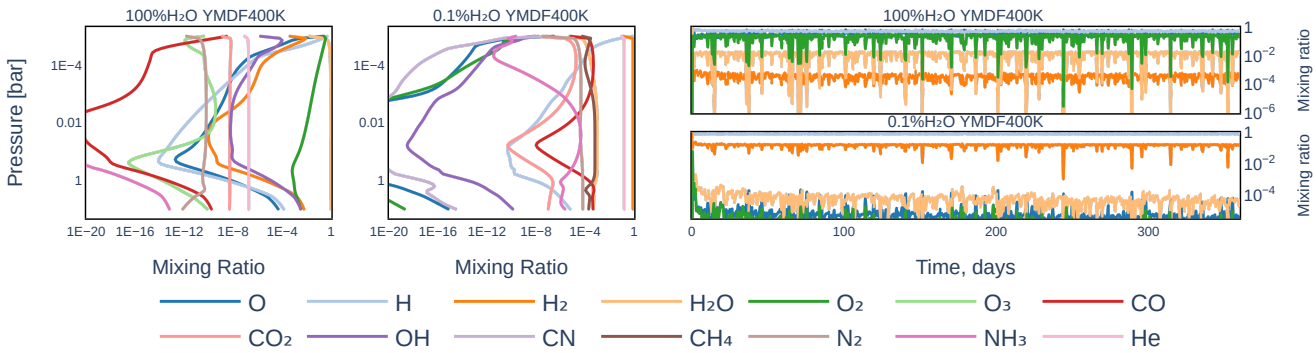

Fig. B.8. Atmospheric mixing ratios for atmospheres with water fractions of 100%, and 0.1% under stellar forcing in the YMDF model and with 400K internal hitting at the bottom boundary (two vertical panels on the left), and 360-days evolution of the mixing ratios of photodissociation-driven species with concentrations above 10^{-4} in the uppermost atmospheric layer of these two atmospheric regimes (two horizontal panels on the right).